General Disclaimer

One or more of the Following Statements may affect this Document

- This document has been reproduced from the best copy furnished by the organizational source. It is being released in the interest of making available as much information as possible.

- This document may contain data, which exceeds the sheet parameters. It was furnished in this condition by the organizational source and is the best copy available.

- This document may contain tone-on-tone or color graphs, charts and/or pictures, which have been reproduced in black and white.

- This document is paginated as submitted by the original source.

- Portions of this document are not fully legible due to the historical nature of some of the material. However, it is the best reproduction available from the original submission.

X-621-71-241

PREPRINT

NASA TM X- 65658

A THREE DIMENSIONAL MODEL OF THERMOSPHERIC DYNAMICS:

II. TIDAL WAVES

H. VOLLAND
H. G. MAYR

JUNE 1971

GSFC

GODDARD SPACE FLIGHT CENTER
GREENBELT, MARYLAND

X-621-71-241

A THREE DIMENSIONAL MODEL OF THERMOSPHERIC DYNAMICS:

II. TIDAL WAVES

by
H. Volland
Astronomical Institutes
University of Bonn
Bonn, Germany

and

H. G. Mayr
Goddard Space Flight Center
Greenbelt, Md., USA

GODDARD SPACE FLIGHT CENTER
Greenbelt, Maryland

A THREE DIMENSIONAL MODEL OF THERMOSPHERIC DYNAMICS:

II. TIDAL WAVES

H. Volland
Astronomical Institutes
University of Bonn
Bonn, Germany

and

H. G. Mayr
Goddard Space Flight Center
Greenbelt, Md., USA

ABSTRACT

The generation and the propagation of three fundamental tidal modes - the symmetric diurnal mode, the symmetric semidiurnal mode and the antisymmetric diurnal mode - have been studied based on a theory outlined in a foregoing paper. The equivalent depths of these modes and the eigenfunctions which describe the latitudinal structure in the pressure field are shown to change with altitude. While within the lower atmosphere the eigenfunctions are the Hough-function they transfer into the ordinary spherical functions at thermospheric heights. The transition occurs between 100 and 200 km. Horizontal winds and pressure amplitudes of the three modes which depend on altitude and latitude are determined and compared with available wind and density data.

1. INTRODUCTION

In the first part of this paper (Volland and Mayr, 1971a; referred to as paper I) we developed a theory of thermospheric dynamics in terms of the eigenfunctions of the dissipative atmosphere. We found approximate general analytic solutions for the generation and propagation of tidal and planetary waves excited by the solar heat input due to XUV-radiation and corpuscular heating. That solar heat input has also been developed in terms of eigenfunctions and contains tidal components (depending on local time) and planetary components (depending on seasonal time). For a quantitative evaluation of the propagation characistics of the various atmospheric wave modes the eigenvalues of the waves must be known. These eigenvalues depend on the equivalent depths which in turn are responsible for the latitudinal structure of the corresponding eigenfunctions. It is the purpose of this paper to calculate the equivalent depths of some of the important tidal modes on an approximate analytic basis and to discuss their height dependence. Planetary waves will be considered in the third part of this paper. A numberical calculation taking account of a more sophisticated thermospheric model will be presented in an additional paper (Volland and Mayr, 1971b; referred to as paper II).

2. APPROXIMATE ANALYTIC EVALUATION OF THE EQUIVALENT DEPTHS

In section 4 of this paper I we determined an analytic solution (Equ. (I/32) for the wave amplitudes of the mode with eigenfunction

$$E_n^{m,f} = \Theta_n^{m,f}(\vartheta, z)\ \exp\left[j\ \left(m\lambda + 2f\Omega t + s\Omega_a t\right)\right] \tag{1}$$

where

$$\Theta_n^{m,f}(\vartheta, z) = \sum_{n'} \delta_{n,n'}^{m,f}(z)\, P_{n'}^{m}(\cos\vartheta)\,. \tag{2}$$

Here, P_n^m are the associated Legendre polynomials in Schmidt's normalization, (r, ϑ, λ) are the spherical co-ordinates, $z=r-R_o$ is the height above the ground, $\bar{f} = \omega/2\,\Omega$ is the Coriolis parameter, ω is the angular frequency of the wave mode, Ω is the frequency of the sidereal day, Ω_a is the frequency of the sidereal year and t is the universal time.

The solution (I/32) can be evaluated provided the eigenvalue and the corresponding equivalent depth of the wave mode are known. The equivalent depth $h_n^{m,f}$ was defined in the usual way (Chapman and Lindzen, 1970) as the solution of the eigenvalue problem of the following set of equations: (see Equs. (I/16) and (I/19)):

$$\begin{aligned}
&jf_u\,\psi_n^{m,f} - \cos\vartheta\,\Phi_n^{m,f} + \frac{1}{2\xi\gamma}\frac{\delta\Theta_n^{m,f}}{\delta\vartheta} = 0\\
&jf_v\,\Phi_n^{m,f} + \cos\vartheta\,\psi_n^{m,f} + \frac{jm}{2\xi\gamma\sin\vartheta}\Theta_n^{m,f} = 0\\
&\frac{1}{\sin\vartheta}\frac{\delta}{\delta\vartheta}\left(\sin\vartheta\,\psi_n^{m,f}\right) + \frac{jm}{\sin\vartheta}\Phi_n^{m,f} + \frac{jx}{2f\xi\gamma}\Theta_n^{m,f} = 0
\end{aligned} \tag{3}$$

where

$$\left.\begin{matrix}\frac{p}{p_o}\\ \frac{u}{c_o}\\ \frac{v}{c_o}\end{matrix}\right\} = \left\{\begin{matrix}\Theta_n^{m,f}\\ \Psi_n^{m,f}\\ \Phi_n^{m,f}\end{matrix}\right\} \frac{P_n^{m,f}(z)}{P_o} \exp\left[j\left(m\lambda + 2\bar{f}\Omega t + s\Omega_a t\right)\right] \tag{4}$$

are the relative wave amplitudes of pressure, northerly wind and westerly wind, and

$$\Psi_n^{m,f} = \frac{j}{2f_u \xi\gamma \sin\vartheta} \sum_{n'} \psi_{n,n'+1}^{m,f} P_{n,n'+1}^{m}$$

$$\Phi_n^{m,f} = -\frac{m}{2f_v \xi\gamma \sin\vartheta} \sum_{n'} \varphi_{n,n'}^{m,f} P_{n'}^{m}$$

are series of sperical harmonics to be determined below. p_o is the mean pressure of the steady state thermosphere, c_o is the velocity of sound $\gamma \sim 1.5$ the ratio between the specific heats,

$$\xi = \frac{\Omega r}{c_o}$$

$$x = \frac{4f^2\Omega^2 r^2}{g\, h_n^{m,f}} \qquad (5)$$

$$f_u = f - j\left(0.6\, Z_{col} + Z_{vis}\right)$$

$$f_v = f - j\left(Z_{col} + Z_{vis}\right) \ ,$$

$$f = \frac{1}{2\Omega}\left(\omega + \Omega_a\right) .$$

Z_{vis} and Z_{col} are the disspiation factors of molecular viscosity and ion-neutral drag (see Equs. (I/3) and (I/4), and g is the earth's acceleration constant.

The latitude dependent part of the eigenfunction in (1), $\Theta_n^{m,f}$, degenerates to the well known Hough-function within the nondissipative atmosphere (Chapman and Lindzen, 1970). It degenerates to the spherical surface P_n^m if the Coriolis force can be neglected (see Equ. (I/23). That is,

surface function P_n^m if the Coriolis force can be neglected (see Equ. (I/23)). That is,

$$\Theta_n^{m,f} \longrightarrow P_n^m$$

$$\delta_{n,n'}^{m,f} \longrightarrow \begin{cases} 1 & \text{for } n' = n \\ 0 & \text{for } n' \neq n \end{cases} \qquad (6)$$

Because of Equ. (6), we shall adopt the following definition for the numbering and the normalization of the eigenfunction $\Theta_n^{m,f}$: the wave domain numbers (n, m) of the eigenfunction $\Theta_n^{m,f}$ shall pass over into the wave domain numbers (n, m) of the corresponding spherical function P_n^m if $|f_u|$, $|f_v| \gg 1$. The normalization of $\Theta_n^{m,f}$ is such that $\delta_{n,n}^{m,f} = 1$. Then, in the case of a highly dissipative atmosphere, the function $\Theta_n^{m,f}$ approaches the form (6). It should be mentioned that our numbering and normalization differs from other definitions of the tidal Hough-function (e. g., Chapman and Lindzen, 1970; Tarpley, 1970).

An exact numerical determination of the equivalent depth $h_n^{m,f}$ can be found from Equs. (3) applying the usual expansion procedure (Chapman and Lindzen, 1970) though our system is mathematically somewhat more diffucult due to the dissipation factots Z. Within the thermosphere the dissipation factors Z increase with altitude and ultimately dominate the Coriolis force if $|Z| \gg 1$. That is generally the case above 200 km altitude where the eigenfunction $\Theta_n^{m,f}$ in fact approaches rather well the associated Legendre polynomial P_n^m (see Fig. 1). Therefore, we shall adopt in this paper an approximate

method to find from the system(3) analytic solutions of the equivalent depths which sufficiently well converge to the corresponding values for the non-dissipative atmosphere or to the formulae of the equivalent depths of Equ. (I/26) in the case of a highly dissipative atmosphere. We do this in the following manner: We apply the assumption for the eigenfunctions of Equ. (1) with the normalization from Equ. (6). We retain the two first equations of (3), but replace the third equation of (3) by

$$\frac{1}{\sin\vartheta}\frac{\delta}{\delta\vartheta}\left\{\text{sinv}\ \Psi_n^{m,f}\right\} - \frac{j\,m\,\Phi_n^{m,f}}{\sin\vartheta} = -\frac{jx}{2f\xi\gamma}\,P_n^m \qquad (7)$$

Since the Hough-functions are tabulated, we can compare those exact data with our approximate calculations in the case of zero dissipation. It will turn out that the Hough-functions are sufficiently well represented in our procedure while the equivalent depths differ by not more than 20% when compared with the exact values. Moreover, our wind fields, though very similar in the latitudinal structure, differ somewhat from the exact structure. In view of the advantages of simple analytic solutions which allow to discuss carefully the dependence of the eigenfunctions on heights, frequency and dissipation we shall, however, tolerate these differences. The exact treatment will certainly modify our approximated results, however, it will not change their substance. We should add that this approach is valid only for the lowest zonal wave domain numbers n.

In the next section we shall calculate explicitly the eigenfunctions and the equivalent depths for some of the important tidal modes. There we shall restrict

ourselves to those tidal modes which appear to be generated most intensively at thermospheric heights (see Eq. (I/9)) and which form the predominant terms in the series of spherical functions for the observed temperature distribution (see Eq. (I/14)). These tidal waves are (in our notation) the symmetric diurnal mode $\Theta_1^{1,1/2}$, the antisymmetric diurnal mode $\Theta_2^{1,1/2}$ and the symmetric semidiurnal mode $\Theta_2^{2,1}$ which degenerate at thermospheric heights into the spherical functions P_1^1, P_2^1 and P_2^2. We shall study the change of their latitudinal structure with height and their propagation characteristics.

3. SYMMETRIC DIURNAL TIDAL MODE $\Theta_1^{1,1/2}$

3a Eigenfunction and quivalent depth

The method to solve the eigenvalue problem of Equ. (3) has been described in some detail for the fundamential diurnal mode called the (1, -1) mode by Kato (1966) or the (1, -2) mode by Lindzen (Chapman and Lindzen, 1970). That mode has been discovered independently by Kato (1966) and Lindzen (1966). It is a trapped mode within the lower atmosphere and the main generator for the geomagnetic Sq current (Stening, 1969; Tarpley, 1970). It plays a dominant role within the thermosphere (Volland and Mayr, 1970). We shall see in the following that in our notation this mode is the $\Theta_1^{1,1/2}$ -mode.

From the tables of the Hough-functions (Chapman and Lindzen, 1970) we find an expension into spherical functions of the diurnal (1, -2) mode of

$$\Theta(1,-2) = 0.777\ P_1^1 + 0.582\ P_3^1 + 0.0751\ P_5^1 + \ldots \qquad (8)$$

where the neglected terms are of the order of 5% and smaller. In order to approximate this Hough-function we start from an expension.

$$\Theta_1^{1,f} = P_1^1 + \delta_{1,3}^{1,f} P_3^1 \tag{9}$$

where we already used our numbering and normalization cheme from Eq. (6). For $f = 1/2$ (solar diurnal component) and $Z = 0$ (nondissipative atmosphere), our eigenfunction (9) should converge sufficiently well to Eq. (8). We futhermore assume for the series of the horizontal winds in (4)

$$\Psi_1^{1,f} = j \frac{\psi_{1,2}^{1,f}}{2f_u \xi\gamma} \frac{P_2^1}{\sin\vartheta}$$

$$\Phi_1^{1,f} = -\frac{1}{2f_v \xi\gamma \sin\vartheta} \left(\varphi_{1,1}^{1,f} P_1^1 + \varphi_{1,3}^{1,f} P_3^1 \right) . \tag{10}$$

Finally, we set for convenience

$$f_u \sim f_v \sim f_k \tag{11}$$

in (3). This restriction will be abandoned in the numerical treatment of paper II.

Substituting Eqs. (9) and (10) into the first two Eqs. (3), we find after some calculation the exact solution

$$\psi_{1,2}^{1,f} = f_k \left(f_k + 1/3 \right) / \left(\sqrt{3}\Delta \right) \longrightarrow -\frac{25\sqrt{3}}{27}$$

$$\varphi_{1,1}^{1,f} = f_k \left(f_k - 7/15 \right) / \Delta \longrightarrow -1/9$$

$$\varphi_{1,3}^{1,f} = \frac{2\sqrt{6}}{15\Delta} f_k \longrightarrow -4\sqrt{6}/9 \tag{12}$$

$$\delta_{1,3}^{1,f} = \frac{2\sqrt{6}}{45\Delta} \longrightarrow 8\sqrt{6}/27$$

with $$\Delta = f_k^2 - 2 f_k /3 - 1/15 \longrightarrow -3/20$$

Here the numbers on the r.h.s. of (12) have been determined for $f_k = f = 1/2$

Introducing the velocity components of Equ. (12) into Equ. (7) we notice that the r.h.s. of (7) is fulfilled and that the equivalent depth is

$$h_1^{1,f} = \frac{2\Omega^2 r^2 f \quad \Delta}{g\left(f_k - 1/6\right)} \quad . \tag{13}$$

In order to compare our result with the corresponding Hough-function $\Theta(1-z)$ of (8), we set $f_k = f = 1/2$. Then we obtain from (12)

$$\delta_{1,3}^{1,1/2} = \frac{8\sqrt{6}}{27} = 0.725$$

which must be compared with the corresponding number from (8) of

$$\frac{0.582}{0.777} = 0.749 \ .$$

Both numbers differ by not more than 3%. The latitudinal structure of both representations of the Hough-function (1, -2) are plotted on the bottom of Fig. 1a as solid and as dash-dotted lines indicating the excellent approximation of our function.

The exact numerical value of the equivalent depth of the(1,-2) mode is

$$h(1,-2) = -\ 12.27 \text{ km (Chapman and Lindzen, 1970).}$$

We compare that number with our value from (13)

$$h_1^{1,1/2} = -\frac{9\Omega^2 r^2}{20\ g} = -\ 9.9 \text{ km} \qquad \text{for } r = R_o \text{ and } f_k = f = 1/2$$

which is about 20% smaller than the exact value. That difference could be compensated in principle by a virtual earth's radius $R_o > R_o$.

The bottom curves in Figs. 1b and 1c show the horizontal wind fields $\Psi_1^{1,1/2}$ and $\Phi_1^{1,1/2}$ for our approximation in the case $f_k = f = 1/2$ (solid lines) and of the exact treatment (dash-dotted lines) thus indicating rather similar latitudinal structures. However, the differences are more pronounced than in the case of the Hough-functions of Fig. 1a.

Within the dissipative thermosphere it is $|f_k| \gg 1$. Thus,

$$\delta_{1,3}^{1,f} \propto 1/\ f_k^{\,2}$$

$$\varphi_{1,3}^{1,f} \propto 1/\ f_k$$

$$;\sqrt{3}\ \ \psi_{1,2}^{1,f} \longrightarrow \varphi_{1,1}^{1,f} \longrightarrow 1\ ,$$

and the wave amplitudes of pressure and horizontal winds indeed approach the formulae of (I/20) to (I/26) where the eigenfunctions degenerate to the ordinary spherical functions.

3b Wind and pressure fields

In order to study the behavior of the eigenfunction within a dissipative atmosphere, we considered a model of the steady state thermosphere of Jacchia (1964) with an exospheric temperature of $T_\infty = 1000^o$ K, and we assumed plausible data of the ion-neutral collision number from a paper of Dalgarno (1964) and dissipation factors Z_{vis} and Z_{hc} from full wave calculations of thermospheric dynamics by Volland and Mayr (1970). The temperature profile and the dissipation factors used are plotted in Fig. 2 versus altitude. Here it must be mentioned that due to our approximations in connection with molecular viscosity, our dissipation factor $Z_{kin} = Z_{col} + Z_{vis}$ becomes ill defined above about 300 km altitude.

Below that height, it is generally $Z_{col} > Z_{vis}$. However, the term Z_{col} decreases with height above 300 km due to the decrease of the electron density. Between 300 and 400 km, the term Z_{col} may therefore fall below the viscosity term Z_{vis}. On the other hand, due to this decrease of Z_{kin}, the horizontal velocity may increase which in turn should lead to an increase of the viscosity term Z_{vis}. For convenience, we therefore assume that Z_{kin} remains constant above 300 km altitude. Moreover, we consider an isothermal atmosphere below 100 km.

In Fig. 1a we plotted the eigenfunction $\Theta_1^{1,1/2}$ versus co-latitude ϑ for the four different heights z = 100 km, 150 km, 200 km and 300 km in amplitude (solid lines) and phase (dashed lines). The phase is given in terms of the delay τ_o with respect to $p_1^{1,1/2}$ (in hours) according to

$$\Theta_n^{m,f} = \left|\Theta_n^{m,f}\right| \; e^{-jm\tau_o} \tag{14}$$

We observe in Fig. 1a a transition from the Hough-function at 100 km to the spherical function P_1^1 at 300 km altitude. That transition occurs mainly between 100 and 200 km. The sperical function P_1^1 is an excellent approximation of $\Theta_1^{1,1/2}$ at 300 km with an accuracy of better than 2%. Similary, in Figs. 1c we note a transition in the longitudinal wind function $\Phi_1^{1,1/2}$ from a wind changing sign at $\vartheta = 65^o$ co-latitude at 100 km to a nearly constant wind velocity at 300 km which agrees with the assymptotic value of

$$\Phi_1^{1,1/2} \; \infty \; P_1^1 / \sin\vartheta = 1$$

in Eq. (I/10). The latitudinal wind function $\Psi_1^{1,1/2}$ in Fig. 1b remains unchanged with height in our approach and is proportional to

$$\psi_1^{1,1/2} \propto dP_1^1/d\vartheta = \cos\vartheta$$

However, the amplitudes and phases (here in terms of the time delay with respect to the pressure $p_1^{1,1/2}$) change drastically with height due to the increasing influence of the dissipation factor Z_{kin}.

The equivalent depth $h_1^{1,1/2}$ of Equ. (13) is a measure of the propagation characteristics of the wave mode. Since the equivalent depth has no direct physical meaning we better describe this behavior by the eigenvalue q from Eq. (I/37), the real and the imaginary term of which are responsible for vertical phase velocity and attenuation. The height dependence of an up going wave is given by (see Eq. (I/33))

$$\exp\ -\{(j\alpha + \beta - 1)\ z/2H_o\}\ .$$

The vertical phase velocity can be represented by a vertical wave length of

$$\lambda_z = \frac{4\pi}{\alpha} H_o\ . \qquad (15)$$

In Fig. 3 we plotted the attenuation factor $(\beta - 1)$ and the propagation factor α of the $\Theta_1^{1,12}$ - mode versus altitude. The upper scale in Fig. 3b gives the normalized vertical wavelength λ_z / H_o according to Eq. (15). From Fig. 3 we notice that the $\Theta_1^{1,1/2}$ - mode, while purely evanescent below 100 km ($\alpha = 0$), changes into a quasi - evanescent mode within the thermosphere. Here, wave attenuation reaches a maximum near 140 km and then diminishes below the 100 km-value within the upper part of the thermosphere.

The vertical wavelength is infinite below 100 km. It remains very large (of the order of 1000 km) at thermospheric heights.

From Figs. 1 to 3 we conclude that the thermosphere above about 200 km height as well as the lower atmosphere below 100 km behave nearly like isothermal atmospheres with constant parameters. Therefore our solutions derived in (I/41) and (I/50) can be applied to a sufficient degree of approximation, while the transition region between 100 and 200 km must be treated by full wave theory to be discussed in paper II.

We calculated from (I/48) the generation and propagation of the $\Theta_1^{1,1/2}$ -mode within an isothermal nondissipative lower atmosphere assuming a heat input between the ground and 100 km proportional to the mean pressure:

$$J_1^{1,1/2} = \frac{\kappa Q_1^{1,1/2}}{\Omega p_o} = \begin{cases} -0.01 & \text{for } \leq z \leq 100 \text{ km} \\ 0 & \text{for } > z \quad 100 \text{ km} \end{cases} \tag{16}$$

with the maximum heat input during local noon. We plotted the relative amplitudes of vertical wind w/c_o, pressure p/p_o and temperature T/T_o versus altitude in Figure 4. Though the $\Theta_1^{1,1/2}$ -mode is evanescent ($\beta - 1 = 0.25$) in that height range, the integrated sum of the up- and downgoing waves coherently generated at any height interval below 100 km add together to a net amplitude assymptotically approaching constant values for vertical wind and pressure (see Eq. (I/52b). On the other hand, the temperature decreases, except in the vicinity of 100 km which is the upper boundary of the heat input.

Above 100 km the wave amplitudes decrease like free internal wave according to Eq. (I/50c). This indicates the small penetration depth of evanescent waves which are only significant within the altitude range of

$$\Delta z = \frac{2H_o}{(\beta - 1)} \sim 50 \text{ km} \tag{17}$$

in the case of upgoing free internal waves within the nondissipative lower atmosphere.

The discontinuity of the temperature amplitude at 100 km in Fig. 4a is the result of the abrupt termination of the heat input at this height level in our model. Below 100 km, the temperature amplitude is generated by the heat input and by adiabatic expansion and heat advection due to winds which act like heat sinks (see Eq. (I/31)). Above 100 km, the heat input becomes zero, however the heat sink due to the advection flow remains. Therefore the temperature amplitude has a discontinuity there and its phase changes by 180°. This phenomenon is of course not to be expected in reality since the heat input distribution is actually continuous.

Vertical velocity and temperature have a constant time delay with respect to the solar heat input of 0 h and 6 h, respectively. The pressure changes sign at an altitude of $z_{isop} = 1.8$ km in our model where z_{isob} is the height of a true isobaric layer. Above that height, the pressure peaks at 18 h L. T. like the temperature, below that height it peaks at 6 h L. T.

The horizontal velocity components are proportional to the pressure (see Eq. (4) and therefore have the same vertical distribution.

The latitudinal wind is shifted by 6 h with respect to the pressure and peaks at 0 h L. T. above z_{isob}. The longitudinal wind has the same phase as the pressure.

A noon-midnight meridional cross-section of the global wind system of the $\Theta_1^{1,1/2}$ -mode within the lower atmosphere has been drawn in Fig. 5. The wind rises at the zone of maximum heating on the day time hemisphere, crosses the poles and falls on the night time hemisphere. This wind system is completely equivalent to the circulation cell of a thermally driven wind. The longitudinal winds (with maximum values at 18 h L. T. on the day time hemisphere and at 6 h L. T. on the night time hemisphere) are indicated in Fig. 7 within the various sections of the cell by the symboles E = easterly (blowing from the east) and W = westerly (blowing from the west).

In Fig. 6 we repeated these calculations for thermospheric conditions (using Eq (I/41)). Here we assumed a solar heat input of

$$J_1^{1,1/2} \begin{cases} -0.01 & \text{for} \quad z \geq z_o \\ 0 & \text{for} \quad z < z_o \end{cases} \tag{18}$$

and adopted the temperature and dissipation data at 300 km altitude (see Fig. 2). The range $z_o \leq z \leq z_o + 200$ km in Fig. 6 represents the height region between about 200 and 400 km. As we already mentioned, the general behavior of the $\Theta_1^{1,1/2}$ - mode at thermospheric heights is similar to the situation within the lower atmosphere as shown in Fig. 4. However, there exist some remarkable differences. First, the penetration depth of the quasi-evanescent mode is much greater than the corresponding value of Eq. (17) and of the order of

$$\Delta z \sim 1200 \text{ km} .$$

Therefore, the assymptotic values of pressure and vertical wind indicated by the vertical dashed lines in Fig. 6 are still twice the values at $z-z_o$ = 200 km. Second, the pressure field has a minimum but final value near 4 km above the lower boundary of the heat input. Therefore, a true isobaric layer is not to be expected within the dissipative thermosphere. Moreover, the phase difference between the pressure below and above the quasi-isobaric layer is not greater than 10 h (Fig. 6b) as compared with exactly 12 h within the nondissipative lower atmosphere (Fig. 4).

Within the first 200 km above z_o the phases of pressure, temperature and vertical wind decrease slowly with altitude (Fig. 6b). Below the height z_o which is the lower boundary of the heat input only downgoing free internal waves exist which decay rapidly. This indicates the small influence the thermospheric region exerts on the lower atmosphere.

The horizontal winds are proportional to the pressure and therefore have the same height distribution. The upper scale in Fig. 6a gives the magnitude of the latitutdinal wind at the poles determined from Eqs. (4) and (10). The phase of the winds at the poles which can be derived from Figs. 1b and 1c are plotted in Fig. 6b and give phase delays with respect to the pressure of 11.5 h and 5.5 h, respectively. Above 200 km the northerly wind peaks at about 2 h L. T. The westerly wind, shifted by 6 h, peaks at about 20 h L. T.

The circulation cell due to the heat input above $z_o \sim 200$ km is similar to the cell in Fig. 5. However, the change in sign of the longitudinal wind along one meridian, as indicated in Fig. 5 by the vertical lines at $\vartheta = 60°$, disappears. Moreover, above the quasi-isobaric layer the maximum northerly

wind flows at 2 h L. T. as compared with 0 h L. T. in Fig. 5. The total wind circulation of the $\Theta_1^{1,1/2}$ -mode is the sum of the individual circulation cells generated by the heat inputs within the various height regions including the regions between 100 and 200 km and above 400 km. If the heat input decreases nearly exponentially with height, we except only one fundamental circulation cell with the isobaric layer near the ground. Any individual cell above the fundamental cell can form only within a height range where the heat input has a relative maximum. This may happen within the Ozon layer or above the mesopause.

The results of Figs. 6a and 6b justify our assumption about the height structure of the horizontal winds which was needed for the determination of the dissipation factors Z_{vis} in (I/3).

3b Comparison with experimental data

The numerical results shown in Figs. 1 to 6 are compared with available experimental data. From the work of Kato (1966), Stening (1969), Tarpley (1970) and Volland (1971) it appears to be well established that the $\Theta_1^{1,1/2}$ -mode is the main generator of the geomagnetic Sq current. Its horizontal wind field has the right latitudinal structure to drive the Sq current. The phase of the wind of the $\Theta_1^{1,1/2}$ -mode changes slowly enough with altitude so that the induced electric current densities produce an optimally large magnetic field on the ground. From our result we may conclude furthermore that, provided the solar heat input peaks at local noon, the phase of the latitudinal wind of the $\Theta_1^{1,1/2}$ -mode varies from 0 h L. T. below 100 km to

about 2 h L. T. above 300 km (see Figs. 4 and 6). This is just the phase value necessary in a consistent dynamo theory. Volland (1971) used a phase of u of 0 h L. T. which is the expected phase in the nondissipative atmosphere. Tarpley (1970) assumed a phase of u of 1.3 h L. T. which is a value to be expected above 100 km. We moreover can estimate from the magnitude of the wind velocity necessary to explain the observed geomagnetic Sq variation (which is $u_{max} \sim 120$ m/sec) and from our result in Fig. 4 the normalized heat input of

$$J_1^{1,1/2} \sim -0.05 \tag{19}$$

which is one order of magnitude greater than the corresponding values estimated for the Ozon-layer (Chapman and Lindzen, 1970). Finally it can be shown that the structure of the Sq current changes only slightly if the wind field of the $\Theta_1^{1,1/2}$ -mode changes with height according to Fig. 1b and 1c.

We now compare our results of Figs. 1 to 6 with available satellite drag data. As it is obvious from Eqs. (I/9) and (I/13), the predominant diurnal component of density and temperature variations within the thermosphere correspond to the fundamental heat input component P_1^1. Assuming a maximum heat input during local noon, the component of the density and temperature variation peaks with a time delay of about 3 h at 15 h L. T. Both latitudinal structure and time delay of the diurnal component are completely consistent with our result given in Figs. 1 and 6.

The experimental facts, namely the tendency of an increasing relative pressure amplitude with height approaching an assymptotic value and the nearly isothermal behavior of the thermosphere are also indicated in Fig. 6.

Here, we should mention again that our temperature values appear to be underestimated. Especially, the slow decrease of the temperature amplitude with height is not realistic. This results from the neglect of heat conduction waves which play an increasingly significant role at thermospheric heights (see the results of full wave calculation in paper II and the paper by Volland and Mayer (1970)).

For a comparison between the relative pressure amplitude in Fig. 6 and corresponding abservational data (e.g., Jacchia 1965) we have to take into account that a pressure component generated by a heat input below $z_o \sim 200$ km height must be added to the pressure amplitude in Fig. 6 to obtain the total observed pressure variation (Volland and Mayr, 1970). The total pressure amplitude at 400 km height may therefore have reached nearly the assymptotic value indicated by the vertical dashed line. Taking a total pressure amplitude at 400 km of about 2/3 of the assymtotic value in Fig. 6 and comparing it with the observed relative pressure amplitude of about 0.5 at 400 km we find a normalized heat input of

$$J_1^{1,1/2} \sim -0.1 \tag{20}$$

which is not inconsistent with the result of Eq. (19).

The average height integrated heat input per area necessary to generate the observed density amplitude at the thermospheric heights can be estimated from Eqs. (I/9) and (I/27). It is for the diurnal component

$$2\, Q_{XUV}^{o} \sim -\frac{\Omega\, p_o}{\kappa}\, J_1^{1,1/2} \quad .$$

Thus it is

$$\frac{\overline{Q}_{XUV}}{4\pi r_o^2} = Q^o_{XUV}\ H_o \sim -\frac{\Omega p_o H_o}{2\kappa}\ J_1^{1,1/2} \sim 1\ \text{erg/cm}^2\ \text{sec}$$

above 120 km height with $p_p \sim 2.6 \times 10^{-2}$ erg/cm^3 at 120 km altitude, $H_o \sim 40$ km and $J_1^{1,1/2}$ from Eq. (20). This is a plausible number for the effective solar XUV heat input within a column above 120 km height (Hinteregger et al., 1965).

Finally, it can be shown that the horizontal wind structure of the $\Theta_1^{1,1/2}$ -mode at 300 km altitude is essentially identical with the wind fields derived from Jacchia's pressure fields (Jacchia and Slowey 1967) by Geisler (1967) and Kohl and King (1967).

4. THE ANTISYMMETRIC DIURNAL TIDAL MODE $\Theta_2^{1,1/2}$

4a Eigenvalue and equivalent depth

The antisymmetric diurnal tidal mode $\Theta_2^{1,1/2}$ which degenerates to the spherical function P_2^1 at thermospheric heights is according to Eqs. (I/9) and (I/13) the most important antisymmetric diurnal mode and describes the annual modulation of the diurnal variation of the solar heat input and its corresponding density variation which is proportional to

$$\Theta_2^{1,1/2}\ \cos\tau\ \cos\Omega_a t\ .$$

It will be shown in this section that within the lower nondissipative atmosphere that mode also degenerates to the spherical function P_2^1.
It is known from the work of Hough (1898) that the spherical function P_2^1

must be added to the set of Hough functions to make the system complete. Therefore, P_2^1 indeed is itself a Hough function within the nondissipative atmosphere. In order to study its dependence on altitude, we proceed in a manner outlined in section 3a and start from the expressions

$$\begin{aligned}
\Theta_2^{1,f} &= P_2^1 + \delta_{2,4}^{1,f}\, P_4^1 \\
\Psi_2^{1,f} &= \frac{i}{2f_u \xi\gamma \sin\vartheta}\left(\psi_{2,1}^{1,f}\, P_1^1 + \psi_{2,3}^{1,f}\, P_3^1\right) \\
\Phi_2^{1,f} &= -\frac{1}{2f_v \xi\gamma \sin\vartheta}\left(\varphi_{2,2}^{1,f}\, P_2^1 + \varphi_{2,2}^{1,f}\, P_4^1\right).
\end{aligned} \tag{21}$$

This set of equations fulfilles again exactly the two first equations of (3) and leads to the relationship (with again $f_u = f_v = f_k$)

$$\begin{aligned}
\Psi_{2,1}^{1,f} &= -3\sqrt{3}\, f_k \left(f_k^3 - f_k^2/12 - f_k + 1/12\right) / (5\Delta) \longrightarrow -\sqrt{3} \\
\psi_{2,3}^{1,f} &= 4\sqrt{2}\, f_k \left(f_{kin} + 1/4\right)\left(f_k^2 + f_k/2 - 1/2\right) / (5\Delta) \longrightarrow 0 \\
\varphi_{2,2}^{1,f} &= f_k \left(f_k^3 + 3f_k^2/28 - 4f_k/7 + 9/28\right) / \Delta \longrightarrow -1 \\
\varphi_{2,4}^{1,f} &= 12\sqrt{\frac{10}{3}}\, f_k \left(f_k^2 + f_k/2 - 1/2\right) / (35\Delta) \longrightarrow 0 \\
\delta_{2,4}^{1,f} &= -3\sqrt{\frac{10}{3}}\left(f_k^2 + f_k/2 - 1/2\right) / (35\Delta) \longrightarrow 0
\end{aligned} \tag{22}$$

with

$$\Delta = f_k^4 + f_k^3/4 - 27\, f_k^2/28 - 3\, f_k/28 + 3/28 \longrightarrow -3/32$$

where again the r. h. s. of (22) is determined for $f_k = f = 1/2$. From (22) and (7) we find an equivalent depth of

$$h_2^{1,f} = \frac{2f\Omega^2 r^2 \Delta}{3g\left(f_k - 1/12\right)\left(f_k^2 + f_k/2 - 1/2\right)} \longrightarrow \infty \tag{23}$$

which becomes infinite for the diurnal component ($f_{kin} = f = 1/2$) within the nondissipative atmosphere.

As it is clear from Eqs. (3), (7) and (22), our solution for the Hough function is exact within the nondissipative atmosphere and gives $\Theta_2^{1,1/2} \longrightarrow P_2^1$. Within the dissipative atmosphere it is for $|f_k| \gg 1$

$$\begin{aligned} \delta_{2,2}^{1,f} &\propto 1/f_k^2 \qquad & \varphi_{2,2}^{1,f} &\longrightarrow 1 \\ & \text{and} & & \\ \varphi_{2,4}^{1,f} &\propto 1/f_k \qquad & \psi_{2,1}^{1,f} &\longrightarrow -3\sqrt{3}/5 \; ; \; \psi_{2,3}^{1,f} \longrightarrow 4\sqrt{2}/5 \end{aligned} \tag{24}$$

approaching the formulae (I/20) and (I/26) (Note that

$$\frac{dP_2^1}{d\vartheta} = \frac{1}{5\sqrt{3}\sin\vartheta}\left(4\sqrt{6}\; P_3^1 - 9\; P_1^1\right)$$

4b Wind and pressure fields

In order to study the behavior of the $\Theta_2^{1,1/2}$ -mode within the atmosphere we did the same calculations as in section 3b and plotted in Fig. 7a the eigenfunction $\Theta_2^{1,1/2}$ versus co-latitude for four different heights in amplitude and phase. Here we note a significant deviation from the structure of P_2^1 only within the height range between 100 and 200 km. Figs. 7b and 7c give the wind function $\Psi_2^{1,1/2}$ and $\Phi_2^{1,1/2}$ versus co-latitude for the four heights considered. Here too a transition region exists between 100 and 200 km. Above and below this region the structure of the longitudinal wind is the same and proportional to

$$P_2^1 / \sin\vartheta = \sqrt{3}\cos\vartheta$$

However the structure of the latitudinal wind changes from

$$P_1^1 / \sin\vartheta = 1$$

within the lower atmosphere to a structure proportional to

$$\frac{dP_2^1}{d\vartheta} = \sqrt{3}\left(2\cos^2\vartheta - 1\right)$$

within the upper part of the thermosphere.

The propogation factor α and the attenuation factor $\beta - 1$ of the $\Theta_2^{1,1/2}$ -mode are plotted in Fig. 3. We observe a strong increase of the attenuation factor between 100 and 200 km and then a slow decrease with height.

The attenuation factor $\beta - 1$ is greater by a factor of about 3 than the corresponding value of the $\Theta_1^{i,1/2}$ -mode.

We also did calculations of the generation and propogation of the $\Theta_2^{1,1/2}$ -mode within the lower atmpsphere (Fig. 8) and within the thermosphere (Fig. 9) adopting the same assumptions as in section 3b. We assumed a solar heat input of

$$J_2^{1,1/2} = -0.01$$

below 100 km in Fig. 8 and above $z_o \sim 200$ km in Fig 9 which is equivalent to maximum heating at local noon during northern summer (June-solstice). In the case of the nondissipative atmosphere our solution of the eigenvalue q (I/37) degenerates to

$$q_2^{1,1/2} = -jA \qquad (25)$$

because of $h_2^{1,1/2} \rightarrow \infty$. Thus, we find from (I/50)

$$\begin{aligned} F_a &= -2jA \\ F_b &= 2jA(\gamma - 1) \\ G_a &= -\frac{J}{A(\epsilon - 1)} \\ G_b &= 0 \end{aligned} \tag{26}$$

which means, no downgoing wave is generated. For the upgoing wave we find with $\epsilon = 1$:

$$\lim_{\epsilon \rightarrow 1} a(z) = k_o J z$$

and

$$\begin{aligned} w/c_o &= k_o J z \\ p/p_o &= -2jAk_o J z \\ T/T_o &= -jJ \end{aligned} \tag{27}$$

Within the lower atmosphere, this mode behaves like a degenerated evanescent mode with constant phase, however with the relative amplitude of the pressure linearily increasing with height (see Fig. 8).

Within the termosphere (Fig. 9) the $\Theta_2^{1,1/2}$ -mode behaves like a quasi-evanescent mode and is similar to the $\Theta_1^{1,1/2}$ -mode in Fig. 6. However, there exists one striking difference. As we note from Fig. 3, the attenuation factor $\beta - 1$ of the $\Theta_2^{1,1/2}$ -mode is much greater than the corresponding value of the $\Theta_1^{1,1/2}$ -mode Therefore the penetration depth Δz (see Equ. (17)) is much smaller, and the assymptotic values of vertical wind and pressure (indicated by vertical bars in Fig. 9a) are reached at a lower height than

in the case of Fig. 6a. On the other hand, the magnitudes of the assymptotic values are not affected by the attenuation factors (see Eq. (I/47) and the vertical dashed lines).

The circulation cells corresponding to the heat inputs within the lower atmosphere (Fig. 8) and within the thermosphere (Fig. 9) are shown in Figs. 10a and 10b. Both cells differ significantly from each other. Within the lower atmosphere the isobaric layer is the ground. Thus, only one cell extended over the entire globe is formed, no return wind exists and the latitudinal wind blows from south to north during northern summer and noon. A westerly wind (directed toward the east) blows on the northern day time hemisphere at 18 h L. T. Within the thermosphere (Fig. 10b), two cells on each hemisphere are formed separated from each other at latitudes ± 45°. These winds change their direction during northern winter.

4c Comparison with experimental data

We now want to compare the results of the forgoing sections with available data. From an analysis of the geomagnetic Sq variations, Volland (1971) derived an antisymmetric wind field at E-layer heights which has the exact form of the wind of the tidal $\Theta_2^{1,1/2}$ -mode given in Figs. 7b and 7c at z = 100 km. The wind velocity at the poles was determined to be

$$\left| u_2^{1,1/2} \right| = 20 \text{ m/sec}$$

The phase of the latitudinal wind during northern summer was 0 h L. T. which agrees with the phase of $u_2^{1,1/2}$ plotted in Figs. 8 and 10a if the heat

input peaks at local noon. The ratio between the antisymmetric and the symmetric diurnal winds derived from the Sq current was

$$\left.\frac{u_2^{1,1/2}}{u_1^{1,1/2}}\right|_{\vartheta=0} = \frac{p_2^{1,1/2}}{p_1^{1,1/2}} = \frac{20}{\sqrt{3}\ 105} = 0.11 \qquad (28)$$

From the Jacchia model (Jacchia and Slowey 1964) we find a (2,1)-component of the exospheric temperature (Eq. (I/14)) of

$$\frac{T_2^1}{T_1^1} = \frac{p_2^1}{p_1^1} = \frac{0.008}{0.12} = 0.07 \qquad (29)$$

and a phase value for T_2^1 (that is: of the pressure component p_2^1) of 15 h L. T.*

This phase agrees sufficiently well with the value of 14 h L. T. in our theory (see Fig. 9b). We compare the amplitude ratio of (29) with the corresponding value in our theory which gives

$$\frac{T_2^{1,1/2}}{T_1^{1,1/2}} = \frac{p_2^{1,1/2}}{p_1^{1,1/2}} \sim \frac{1}{3}\ \frac{J_2^{1,1/2}}{J_1^{1,1/2}} \sim \frac{1}{3}\ \frac{5\sqrt{3}}{2 \times 8}\ \delta_o = 0.14 \qquad (30)$$

---

*Note that Jacchia's exospheric temperature represents merely the density amplitude above about 200 km. A relative temperature amplitude in the Jacchia-mode of $T_n^M/T_o = 0.1$ corresponds to a relative density amplitude of $\rho_n^m/\rho_o \sim 0.4$. Moreover, the density amplitude is proportional to the pressure amplitude, and it is $\rho_n^m/\ \rho_o \sim 0.85\ p_n^m/p_o$ within thermospheric heights above 200 km (see also Equ. (I/45)).

Here, for the heat input components we use the XUV-values in (I/9), (I/27) and (I/47). This number is greater by a factor of two than the experimental value in (29) but it appears to be sonsistent with the number of (28)

Considering this discrepancy, we should take into account that the Jacchia-model is based on a plausible but arbitrary temperature and therefore pressure profile which is fixed for all possible frequencies of the disturbance, which is our notation means, fixed for all wave domain numbers (n, m, f). As we may notice from Figs. 6a and 9a, this is certainly not the case. The temperature and pressure profiles strongly depend on the wave domain numbers. Moreover, the exospheric temperature distribution of the Jacchia-model is described by an arbitrary analytic function which appears to fit well the main components like the symmetric diurnal (1,1)-component, but which may more or less deviate from second order components like the antisymmetric diurnal (2,1)-component.

On the other hand, the heat input distribution in Eq. (I/9) based on rather crude assumptions as well as our simplified theory can of course give only first order approximations. In view of these uncertainties, the numbers given in (28), (29) and (30) appear to be quite consistent with each other agreeing completely in phase and leading to an amplitude ratio between the antisymmetric and the symmetric diurnal component of the order of 0.1.

5. SYMMETRIC SEMIDIURNAL TIDAL MODE $\Theta_2^{2,1}$

5a Eigenfunction and equivalent depth

The symmetric semidiurnal tidal mode $\Theta_2^{2,1}$ degenerates within the thermosphere to the spherical function P_2^2 and behaves like a quasi-evanescent mode there. It is responsible for the observed semidiurnal component of the density in Eq. (I/14). Within the lower atmosphere, this mode is a propagation mode called the (2,2) tidal mode in the literature (e.g., Chapman and Lindzen, 1970). It has been tabulated by Chapman and Lindzen and has the following form:

$$\Theta(2,2) = 1.08\ P_2^2 - 0.368\ P_4^2 + 0.044\ P_6^2 + \ldots \tag{31}$$

where the neglected terms are smaller than 3% of the first term. In order to study its height dependence within the nondissipative atmosphere we start in the usual way with the expressions

$$\begin{aligned}
\Theta_2^{2,f} &= P_2^2 + \delta_{2,4}^{2,f}\ P_4^2 \\
\Psi_2^{2,f} &= \frac{j}{2f_u \xi\gamma \sin\vartheta}\ \psi_{2,3}^{2,f}\ P_3^2 \\
\Phi_2^{2,f} &= -\frac{2}{2f_v \xi\gamma \sin\vartheta}\left(\varphi_{2,2}^{2,f}\ P_2^2 + \varphi_{2,4}^{2,f}\ P_4^2\right)
\end{aligned} \tag{32}$$

and obtain from the first two equations in (3) the exact relationship (again with $f_u = f_v\ f_k$)

$$\psi_{2,3}^{2,f} = 2\, f_k \left(f_k + 1/2\right) / \left(\sqrt{5}\Delta\right) \longrightarrow 7/\sqrt{5}$$

$$\varphi_{2,2}^{2,f} = f_k \left(f_k - 5/14\right) / \Delta \longrightarrow 3/2 \qquad (33)$$

$$\varphi_{2,4}^{2,f} = 2\sqrt{15}\ f_k / (35\Delta) \longrightarrow 2/\sqrt{15}$$

$$\delta_{2,4}^{2,f} = -\sqrt{15}/(35\Delta) \longrightarrow -1/\sqrt{15}$$

with

$$\Delta = f_k^2 - f_k/2 - 1/14 \longrightarrow 3/7$$

From (32) and (7) we obtain the equivalent depth of

$$h_2^{2,f} = \frac{2f\,\Omega^2 r^2\,\Delta}{3g\left(f_k - 1/6\right)} \rightarrow \frac{12\,\Omega^2 r^2}{35\,g} = 7.47 \text{ km} \qquad (34)$$

In (32) and (33), the r. h. s. numbers are valid for $f_k = f = 1$.

We can compare the exact numerical value of the (2, 2)-mode which is 7. 85 km (Chapman and Lindzen, 1970) with our approximate value in (33) and find an agreement within about 5%. The bottom curves in Fig. 11a show the exact latitudinal structure of the (2. 2)-mode (dash-dotted line) and our approximated function (31) with the parameters of the r. h. s. of (32) (solid line) and again reveal satisfactory agreement. The bottom curves in Figs. 11b and 11c give the latitudinal and the longitudinal winds functions $\psi_2^{2,1}$ and $\Phi_2^{2,1}$ according to our approximation (solid lines) and according to exact theory for the $\Theta_2^{2,1}$ -mode (dash-dotted lines) within the nondissipative atmosphere. Here too the agreement is sufficient, although not as good as for the eigenfunction $\Theta_2^{2,1}$ itself.

Within the dissipative atmosphere it is for $|f_k| \gg 1$

$$\delta_{2,4}^{2,f} \propto 1/f_k^2 \qquad ; \quad \frac{\sqrt{5}}{2}\,\psi_{2,3}^{2,f} \longrightarrow \varphi_{2,2}^{2,f} \longrightarrow 1 \ ,$$

$$\varphi_{2,4}^{2,f} \propto 1/f_k$$

and the wave amplitudes of pressure and winds again approach the forms of Eqs. (I/20) and (I/26) degenerating to the ordinary spherical functions. (Note that

$$\frac{d\,P_2^2}{d\vartheta} = \frac{2}{\sqrt{5}}\,\frac{P_3^2}{\sin\vartheta}$$

5b. Wind and pressure fields

After repeating the calculations done in sections 3b and 4b we plotted in Fig. 11a the eigenfunction $\Theta_2^{2,1}$ versus co-latitude for the four different heights considered. Above 200 km and below 100 km, the $\Theta_2^{2,1}$ -mode has nearly the same structure with constant phase independent of ϑ. At 150 km, however, we notice a significant phase transition with co-latitude.

In Figs 11b and 11c the wind function $\psi_2^{2,1}$ and $\Phi_2^{2,1}$ are plotted versus co-latitude for the four different heights. Here the structure of the latitudinal wind (Fig. 11b) does not change with height in our approximation and remains proportional to

$$\frac{P_3^2}{\sin\theta} = \sqrt{\frac{15}{4}}\quad \sin\vartheta\quad \cos\vartheta$$

However, the structure of the longitudinal wind changes significantly with height approaching the ϑ-dependence of

$$\frac{P_2^2}{\sin\vartheta} = \sqrt{\frac{3}{4}} \quad \sin\vartheta$$

The propagation factor α and the attenuation factor β-1 of the $\Theta_2^{2,1}$ -mode are plotted in Fig 3. Here, the propagation factor is different from zero at and below 100 km indicating a behavior for this mode resembling a propagation mode. Likewise, the attenuation factor β - 1 is negative below 165 km (the dashed part of the curve in Fig. 3a), corresponding to a net exponential increase with height of the relative wave amplitudes. However, above 165 km the $\Theta_2^{2,1}$ -mode has changed into a quasi-evanescent mode and behaves essentially like the other modes considered.

Simulating lower atmospheric (Fig. 12) and thermospheric (Fig. 13) conditions we calculated the wave amplitudes versus heights due to a heat input of

$$J_2^{2,1} = 0.01$$

which peaks at local noon and at local midnight. Since within the lower atmosphere of scale height H_o = 6 km (the value used in Figs. 4 and 8), the $\Theta_2^{2,1}$ -mode is already a trapped mode, and since we want for illustration to discuss a real propagation mode, we applied a pressure scale height of H_o = 7.8 km in Fig. 12 corresponding to a mean temperature of $T_o = 260^o$ The result of Fig. 12a clearly reveals the characteristics of a propagation mode, namely the exponential increase of the relative wave amplitudes with height apart from the pressure amplitude near the ground where reflection

properties have to be taken into account. Moreover, the phase in Fig. 12b decreases with altitude as we expect from an upward propagating gravity wave. The free internal propagation above 100 km—the termination of the heat input in our model—does not alter that propagation behavior.

The relative amplitudes in Fig. 12a can not increase indefinitely with height in reality. If the relative wave amplitudes approach the value one, our perturbation theory breaks down, and the wave mode will transfer into a shock wave with wave energy dissipation at the shock front. Moreover, higher harmonics of the semidiurnal wave may be generated. On the other hand, within the critical height above 100 km where such transfer may happen, the propagation properties of the $\Theta_2^{2,1}$ -mode change drastically (see Fig. 3) which prevents furthermore an unlimited increase of the wave amplitude. This transition from a propagation mode into a quasi-evanescent mode must be treated by numerical full wave calculations and will be done in paper II. Within the thermosphere (Fig. 13), our wave mode behaves quite normally like a quasi-evanescent mode.

The meridional cross-section of the wind system of the $\Theta_2^{2,1}$ -mode due to the assumed heat input within the thermosphere is given in Fig. 14. Two circulation cells are built up. Maximum latitudinal winds directed to the poles blow at about 7.5 and 19.5 h L. T. above the quasi-isobaric layer z_{isob}. The longitudinal winds, shifted by 2.5 to 3 hours with respect to the latitudinal winds, are westerly at 5 and 17 h L. T. at the equator and above z_{isob} and have the same direction over the entire day time hemisphere.

The wind structure within the lower atmosphere is similar to that of Fig. 14 except for the phase. Here (Fig. 12b), the phase changes continuously with height reaching a phase transition of 180° after about 100 km. Contrary to that behavior, within the thermosphere such transition occurs within a height range of about 20 km (Fig. 13b).

5c Comparison with experimental data

In comparing the result of the forgoing sections with experimental data, we have to take into account that the primary source of the semi-diurnal tidal component is absorption of Ozon in the stratosphere and mesosphere (Bulter and Small, 1963) which means a more complicated vertical structure of the heat input than assumed in Fig. 12. Second, due to the nearly equal values of the pressure scale height and of the equivalent depth of the $\Theta_2^{2,1}$ -mode within the lower atmosphere, the real mean temperature profile is important for the generation and propagation of that mode. E.g., within the mesosphere this mode is evanescent. Therefore, the results in Fig. 12 which were based on an isothermal atmosphere and a constant relative heat input $J_2^{2,1}$ served merely for illustration and cannot be used for a quantitative comparison. More realistic model calculations of the fundamental semidiurnal mode may be found in the book of Chapman and Lindzen (1970).

Since the $\Theta_2^{2,1}$ -mode is partly trapped within the lower atmosphere, the (2,4)-mode (in our notation: the $\Theta_4^{2,1}$ -mode) which is a pure propagation mode throughout the lower atmpsphere may significantly contribute at thermospheric heights. The wind data obtained between 80 and 100 km from

Meteor trail measurements (Elford, 1959 ; Greenhow and Neufield, 1961) which give velocities of the order of 20 m/sec for the semidiurnal component therefore may be related to the $\Theta_4^{2,1}$-mode rather than to the $\Theta_2^{2,1}$-mode (Hines, 1963). Similarly, the evaluation of a sequence of wind measurements at intervals throughout a single night above about 120 km (Murphy and Bull, 1968) leading to vertical wave lengths of 50 - 60 km give further support for the predominance of the $\Theta_4^{2,1}$ -mode at those heights.

On the other hand, within the upper part of the thermosphere the $\Theta_4^{2,1}$ -mode should be suppressed due to its quasi-evanescent behavior like (see Eq. I/47)

$$\left| \frac{p_4^{2,1}}{p_1^{1,1/2}} \right| \sim \frac{1}{10} \left| \frac{J_4^{2,1}}{J_1^{1,1/2}} \right| < \frac{1}{10} \tag{35}$$

and should become insignificant there. This idea is consistent with the density data deduced from satellite drag measurements (see Wq. (I/14)). However, the semidiurnal $\Theta_2^{2,1}$ -mode should be related to the fundamental diurnal $\Theta_1^{1,1/2}$-mode by

$$\left| \frac{p_2^{2,1}}{p_1^{1,1/2}} \right| \sim \frac{1}{3} \left| \frac{J_2^{2,1}}{J_1^{1,1/2}} \right| \sim \frac{1}{3} \quad \frac{5\sqrt{12}}{2 \times 16} = 0.18 \tag{36}$$

if we adopt the numbers given in Eqs. (I/9), (I/27) and (I/47), and the time of maximum of the pressure component of the $\Theta_2^{2,1}$ -mode is about 13 - 13.5 h. L.T. according to Fig. 13b.

We compare these numbers with the experimental result of Eq. (I/1) which gives

$$\frac{T_2^2}{T_1^1} \sim \frac{p_2^2}{p_1^1} \sim \frac{0.035}{0.12} = 0.29 \qquad (37)$$

and a phase T_2^2 of 13.2 h. L. T..

While the observed phase value excellently agrees with the theory, the observed amplitude ratio in (37) is greater by about 50% than the calculated number in (36). This difference can be interpreted as resulting from a relatively strong influence of the wave generated below 200 km where the $\Theta_2^{2,1}$ -mode transfers from a propagation mode into a quasi-evanescent mode. Indeed, Lindzen (1970) calculated that the semidiurnal component from below should be significant at thermospheric heights although according to our theory his result appears to be over-estimated. A final answer to that problem can be given only in a numerical full wave treatment (to be done in paper II) where the transition range between 100 and 200 km must properly be taken into account. Here also the question may be solved why the phase of the semidiurnal component of the neutral temperature derived from Thompson backscatter measurements at 250 km (Mahajan, 1969; Waldteufel and McClure, 1969) is phase shifted by about 2 hours with respect to the corresponding maximum of the density (Volland, 1970).

6. CONCLUSION

Based upon a theoretical treatment of a threedimensional spherical thermospheric model outlined in a previous paper (Volland and Mayr, 1971a)

we determined the eigenfunctions and the equivalent depths of three fundamental tidal modes—the symmetric diurnal mode, the antisymmetric diurnal mode and the symmetric semidiurnal mode—and calculated their dependence on height and latitude within the dissipative thermosphere. The corresponding pressure and horizontal wind fields of these modes have been calculated and meridional cross-sections of the circulation cells due to these modes have been determined. The theoretical magnitude and phase of the wave amplitudes of pressure and horizontal winds of the various tidal wave modes have been compared with corresponding available experimental data and show satisfying agreement. We conclude from this results that a spatial solar XUV heat input distribution within the thermosphere proportional to the solar zenith angle is the main generator of the three tidal waves considered and that the Jacchia-model of the thermospheric density distribution (Jacchia and Slowey, 1967) can readily be interpreted as the thermospheric density response to that energy input.

7. Literature

Butler, S.T. and V. A. Small — 1965 — The excitation of atmospheric oscillations, Proc. Roy. Soc. A 274, 91-121

Chapman, S. and R. S. Lindzen — 1970 — Atmospheric tides, D. Reidel Publ. Comp., Dordrecht-Holland

Dalgarno, A. — 1964 — Ambipolar diffusion in the F-region, J. Atm. Terr. Phys. 26, 939

Elford, W. G. 1959 A study of winds between 80 and 100 km in medium latitudes
Planet. Space Sci. 1, 94-101

Geisler, J. E. 1967 A numerical study of the wind system in the middle thermosphere
J. Atm. Terr. Phys. 29, 1469-1482

Greenhow, J. S. and E. L. Neufeld 1961 Winds in the upper atmosphere
Quart. Journ. Roy. Meteorol. Soc. 87, 564-574

Hines, C. O. 1963 The upper atmosphere in motion
Quart. Journ. Roy. Meteorol. Soc. 89, 1-42

Hinteregger, H. E., L. A. Hall and G. Schmidtke 1965 Solar XUV radiation and neutral particle distribution in July 1963 thermosphere
Space Res. V, pp. 1175-1190

Hough, S. S. 1898 The application of harmonic analysis to the dynamical theory of the tides, Part II,
Phil. Trans. Roy. Soc. London A 191, 139-185

Jacchia, L. G. 1965 Static diffusion models of the upper atmosphere with empirical temperature profiles
Smithsonian Contr. Astrophys. 8, 215-257

Jacchia, L. G. and J. Slowey 1967 The shape and location of the diurnal bulge in the upper atmosphere
Space Res. VII, pp. 1077-1090

Kato, S.	1966	Diurnal atmospheric oscillations Journ. Geophys. Res. 71, 3201-3214
Kohl, H. and J. W. King	1967	Atmospheric winds between 100 and 700 km and their effect on the ionosphere Journ. Atm. Terr. Phys. 29, 1045-1062
Lindzen, R. S.	1966	On the theory of the diurnal tide, Month. Wea.Rev. 94, 295-301
Lindzen, R. S.	1970	Internal gravity waves in atmospheres with realistic dissipation and temperature, Part III: Daily variations in the thermosphere Geophys. Fluid. Dyn. 1,
Mahajan, K. K.	1969	Diurnal variation of the ion temperature Journ. Atm. Terr, Phys. 31, 93-101
Murphy, C. H. and G. V. Bull	1968	Ionospheric winds over Yuma, Arizona, measured by gun-launched projectiles Journ. Geophys. Res. 73, 3005-3015
Stening, R. J.	1969	An assessment of the contributions of various tidal winds to the Sq current system Planet. Space Sci. 17, 889-908
Tarpley, J. D.	1970	The ionospheric wind dynamo, Part II Planet. Space Sci. 18, 1091-1103

Volland, H. 1970 Phase delay between neutral temperature and neutral density at thermospheric heights
Journ. Geophys. Res. 75, 5618-5620

Volland, H. 1971 A simplified model of the geomagnetic Sq current system and the electric fields within the ionosphere
Cosmical Electrodyn, 2, 428-459

Volland H. and H. G. Mayr 1970 A theory of the diurnal variations of the thermosphere
Ann. Geophys. 26, 907-919

Volland H. and H. G. Mayr 1971a A threedimensional model of thermospheric dynamics, Part I: heat input and eigenfunctions

Volland H. and H. G. Mayr 1971b A numerical study of a threedimensional spherical thermospheric density and wind model
in preparation

Waldteufel, P. and J. P. McClure 1969 Preliminary comparison of middle and low latitude Thomson scatter data
Ann. Geophys. 25, 785-793

FIGURE CAPTIONS

Figure 1. Dependence on co-latitude ϑ of the eigenfunction of the symmetric diurnal tidal $\Theta_1^{1,\,1/2}$ -mode for four different heights

Fig. 1a: Pressure function $\Theta_1^{1,\,1/2}$

Fig. 1b: Latitudinal wind function $\psi_1^{1,\,1/2}$

Fig. 1c: Longitudinal wind function $\Phi_1^{1,\,1/2}$

Solid lines: magnitudes

Dashed lines: time delay (in hours)

Dash-dotted lines: exact values within the nondissipative atmosphere

Figure 2. Vertical profiles of mean temperature T_o and dissipation factors due to heat conduction (Z_{hc}), and due to viscosity and ion drag (Z_{kin}) used in our model calculations.

Figure 3. Fig. 3a: Attenuation factors $\beta - 1$ (β is the imaginary part of the eigenvalue). $\beta_2^{2,1} - 1$ is negative below 165 km (the dashed line in Fig. 3a).

Fig. 3b: Propagation factors α (α is the real part of the eigenvalue).

Figure 4. Relative wave amplitudes of pressure p, temperature T and vertical wind w versus altitude of the symmetric diurnal $\Theta_1^{1,\,1/2}$ -mode within the lower nondissipative atmosphere. The latitudinal velocity u is proportional to the pressure. Its pole values are given in the upper right scale. The time delay τ_o gives the time of maximum amplitude in local time. The heat peaks at local

noon and is terminated at 100 km. Therefore above 100 km only upward propagating free internal wave exist. The pressure amplitude is zero at the height of the isobaric layer z_{isob} =1.8 km and shifts in phase by 12 hours there (see the box on the l.h.s.)

Figure 5. Noon-midnight meridional cross-section of the wind system of the tidal $\Theta_1^{1,\ 1/2}$ -mode within the lower atmosphere. The longitudinal winds are phase shifted by 6 hours with respect to the latitudinal winds. Maximum westerly winds (winds blowing from the west) are indicated by the symbol "W", easterly winds (winds blowing from the east) are indicated by "E".

Figure 6. Relative wave amplitudes of pressure p, temperature T and vertical wind w versus altitude of the tidal $\Theta_1^{1,\ 1/2}$ -mode within the dissipative thermosphere $(z_o \sim 200\ km)$. The generating heat input peaks at local noon and is terminated at the height z_o. Below that height only downgoing free internal waves exist.

Fig. 6a: magnitudes (the vertical dashed lines give the maximum asymptotic values of pressure and vertical wind).

Fig. 6b: times of maximum (in hours local time).

Figure 7. Dependence on co-latitude ϑ of the eigenfunction of the antisymmetric diurnal tidal $\Theta_2^{1,\ 1/2}$ -mode for four different heights.

Fig. 7a: Pressure function $\Theta_2^{1,\ 1/2}$

Fig. 7b: Latitudinal wind function $\Psi_2^{1,\ 1/2}$

Fig. 7c: Longitudinal wind function $\Phi_2^{1,\ 1/2}$

Solid lines: magnitude

Dashed lines: time delay (in hours)

Figure 8. Relative wave amplitudes of pressure p, temperature T and vertical wind w versus altitude of the antisymmetric diurnal tidal $\Theta_2^{1,\ 1/2}$ -mode within the lower nondissipative atmosphere and during June-solstice. The generating heat input peaks at local noon and is terminated at 100 km. The time delay τ_o gives the time of maximum amplitude in local time.

Figure 9. Relative wave amplitudes of pressure p, temperature T and vertical wind w versus altitude of the tidal $\Theta_2^{1,\ 1/2}$ -mode within the dissipative thermosphere during June-solstice. The generating heat input peaks at local noon and is terminated at $z_o \sim 200$ km.

Fig. 9a: magnitudes (the vertical dashed lines give the maximum assymptotic values of pressure and vertical wind).

Fig. 9b: times of maximum (in hours local time).

Figure 10. Meridional cross-section of the wind system of the tidal $\Theta_2^{1,\ 1/2}$ -mode during June-solstice within the lower atmosphere and within the thermosphere. Maximum longitudinal winds phase shifted by about 6 h with respect to the meridional winds are indicated by "W" (westerly winds) and by "E" (easterly winds).

Figure 11. Dependence on co-latitude ϑ of the eigenfunction of the symmetric semidiurnal tidal $\Theta_2^{2,\ 1}$ -mode for four different heights.

Fig. 11a: Pressure function $\Theta_2^{2,\ 1}$

Fig. 11b: Latitudinal wind function $\Psi_2^{2,\ 1}$

Fig. 11c: Longitudinal wind function $\Phi_2^{2,\,1}$

Solid lines: magnitudes

Dashed lines: time delay (in hours)

Dash-dotted lines: exact values within the nondissipative lower atmosphere.

Figure 12. Relative wave amplitude in magnitude (Fig. 12a) and time of maximum in hours L. T. (Fig. 12b) of pressure p, temperature T and vertical wind w versus altitude of the symmetric semidiurnal tidal $\Theta_2^{2,\,1}$ -mode within the lower nondissipative atmosphere. The longitudinal wind v is proportional to the pressure. Its equator values are given in the upper right scale. The generating solar heat input peaks at local noon and midnight and is terminated at 100 km.

Figure 13. Relative wave amplitudes in magnitude (Fig. 13a) and time of maximum in hours local time (Fig. 13b) of pressure p, temperature T and vertical wind w versus altitude of the tidal $\Theta_2^{2,\,1}$ -mode within the dissipative thermosphere. The generating solar heat input peaks at local noon and midnight and is terminated at $z_o \sim 200$ km.

Figure 14. Meridional cross-section of the wind system of the tidal $\Theta_2^{2,\,1}$ -mode within the thermosphere. Maximum longitudinal winds phase shifted by about 3 hours with respect to the latitudinal winds are indicated by "W" (westerly winds) and by "E" (easterly winds).

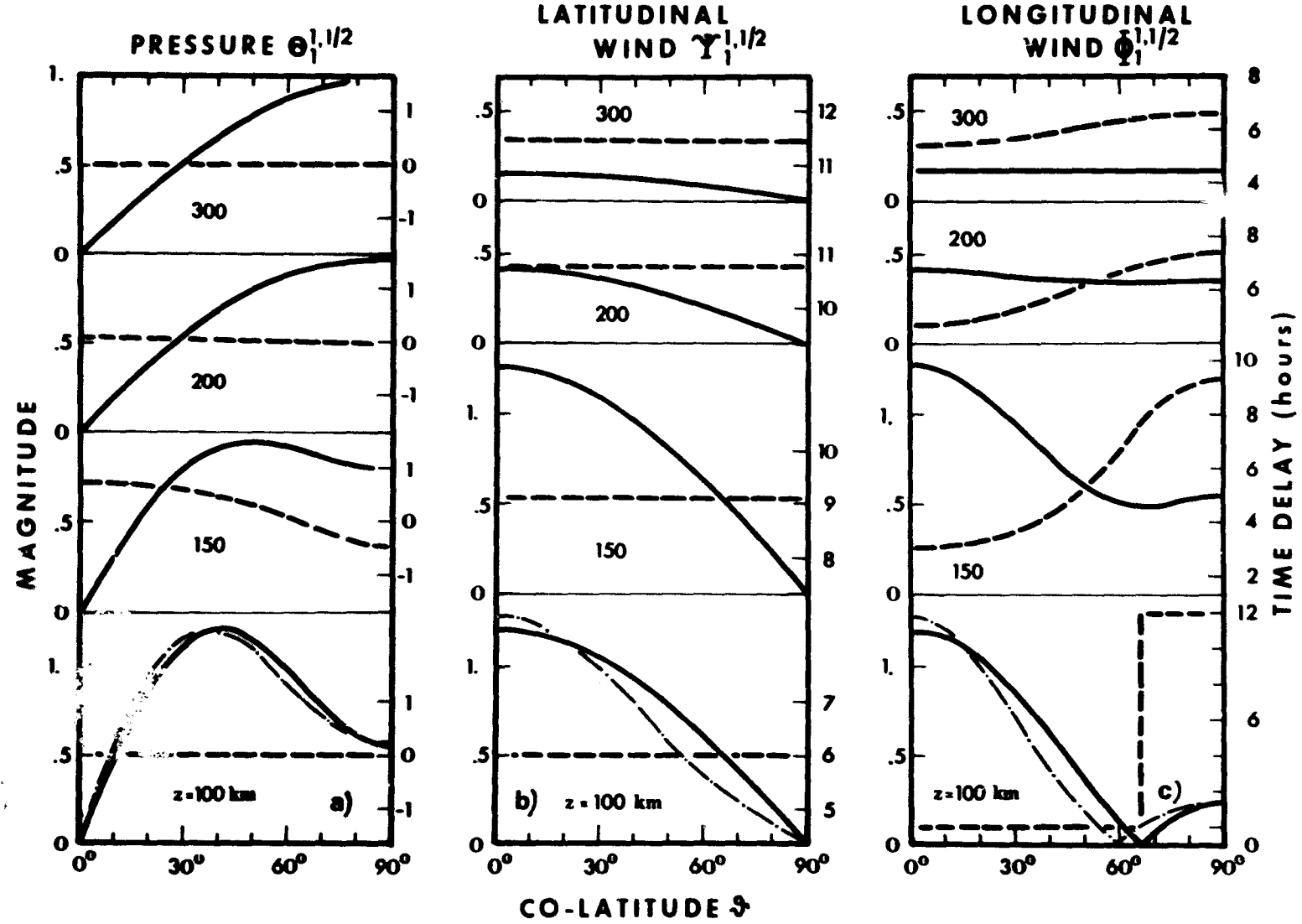

Figure 1. Dependence on co-latitude ϑ of the eigenfunction of the symmetric diurnal tidal $\Theta_1^{1,1/2}$ -mode for four different heights
Fig. 1a: Pressure function $\Theta_1^{1,1/2}$ Fig. 1b: Latitudinal wind function $\Psi_1^{1,1/2}$ Fig. 1c: Longitudinal wind function $\Phi_1^{1,1/2}$

Solid lines: magnitudes Dashed lines: time delay (in hours) Dash-dotted lines: exact values within the nondissipative atmosphere

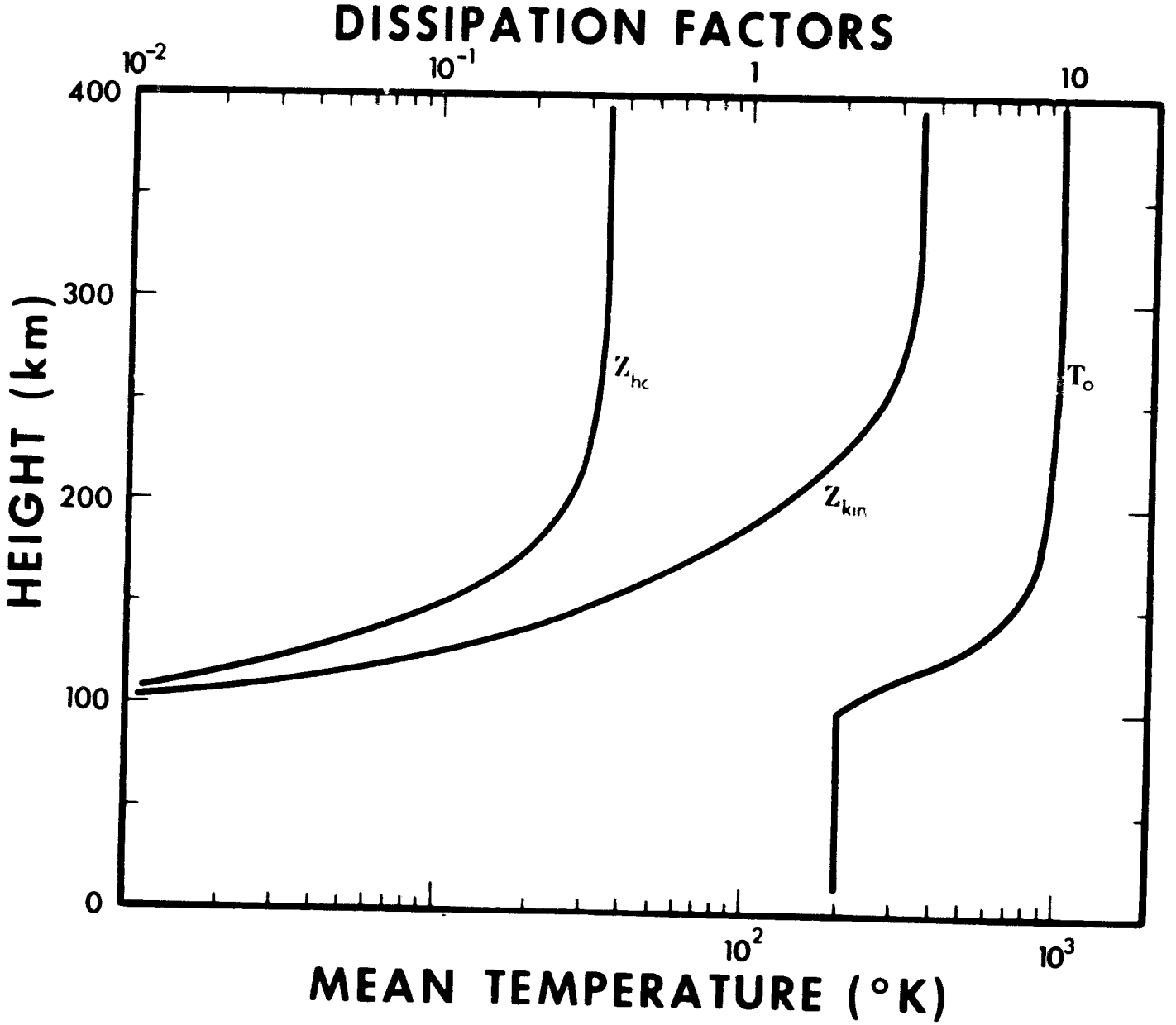

Figure 2. Vertical profiles of mean temperature T_o and dissipation factors due to heat conduction (Z_{hc}), and due to viscosity and ion drag (Z_{kin}) used in our model calculations.

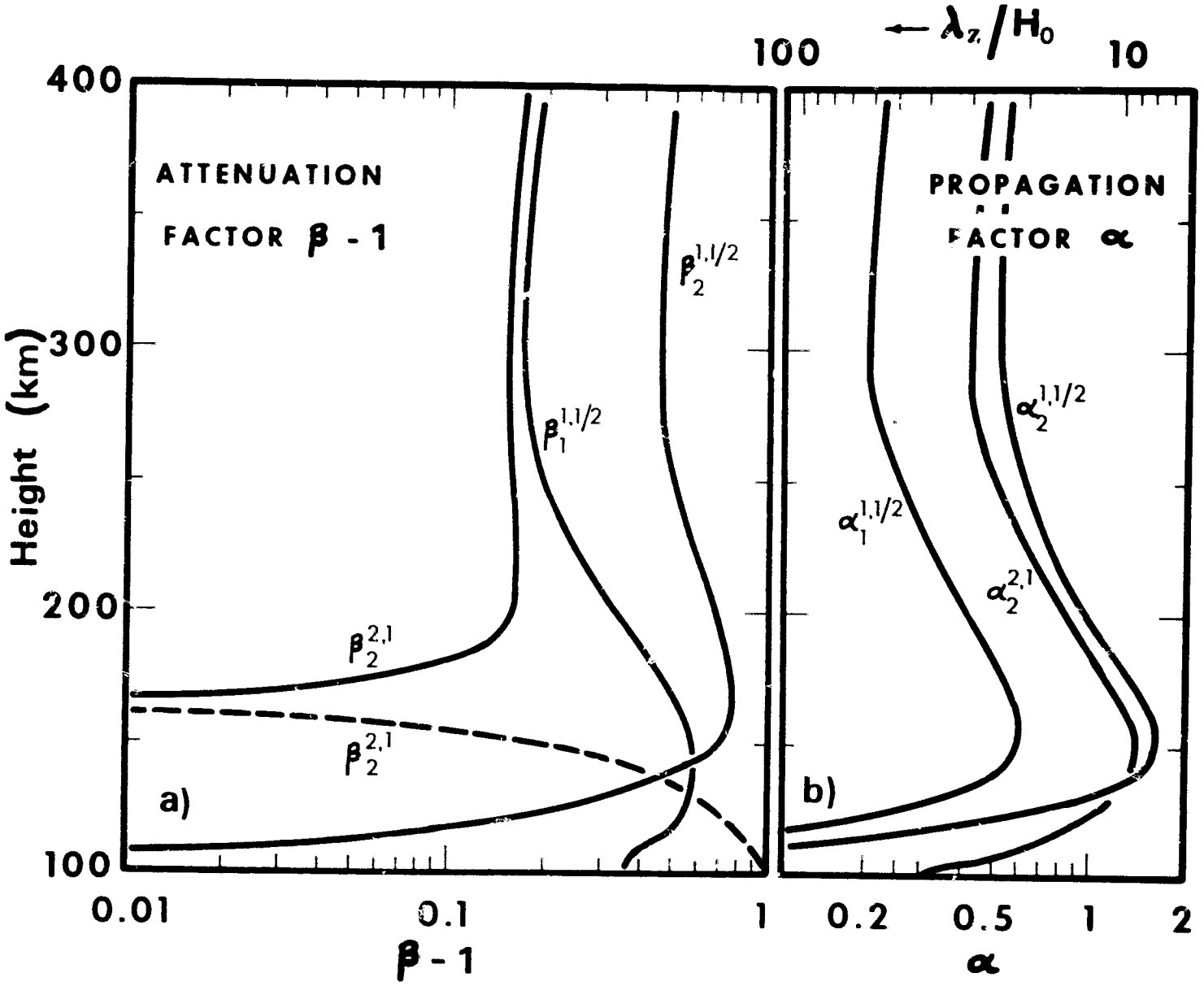

Figure 3. Fig. 3a: Attenuation factors β-1 (β is the imaginary part of the eigenvalue). $\beta_2^{2,1}$ -1 is negative below 165 km (the dashed line in Fig. 3a).
Fig. 3b: Propagation factors α (α is the real part of the eigenvalue).

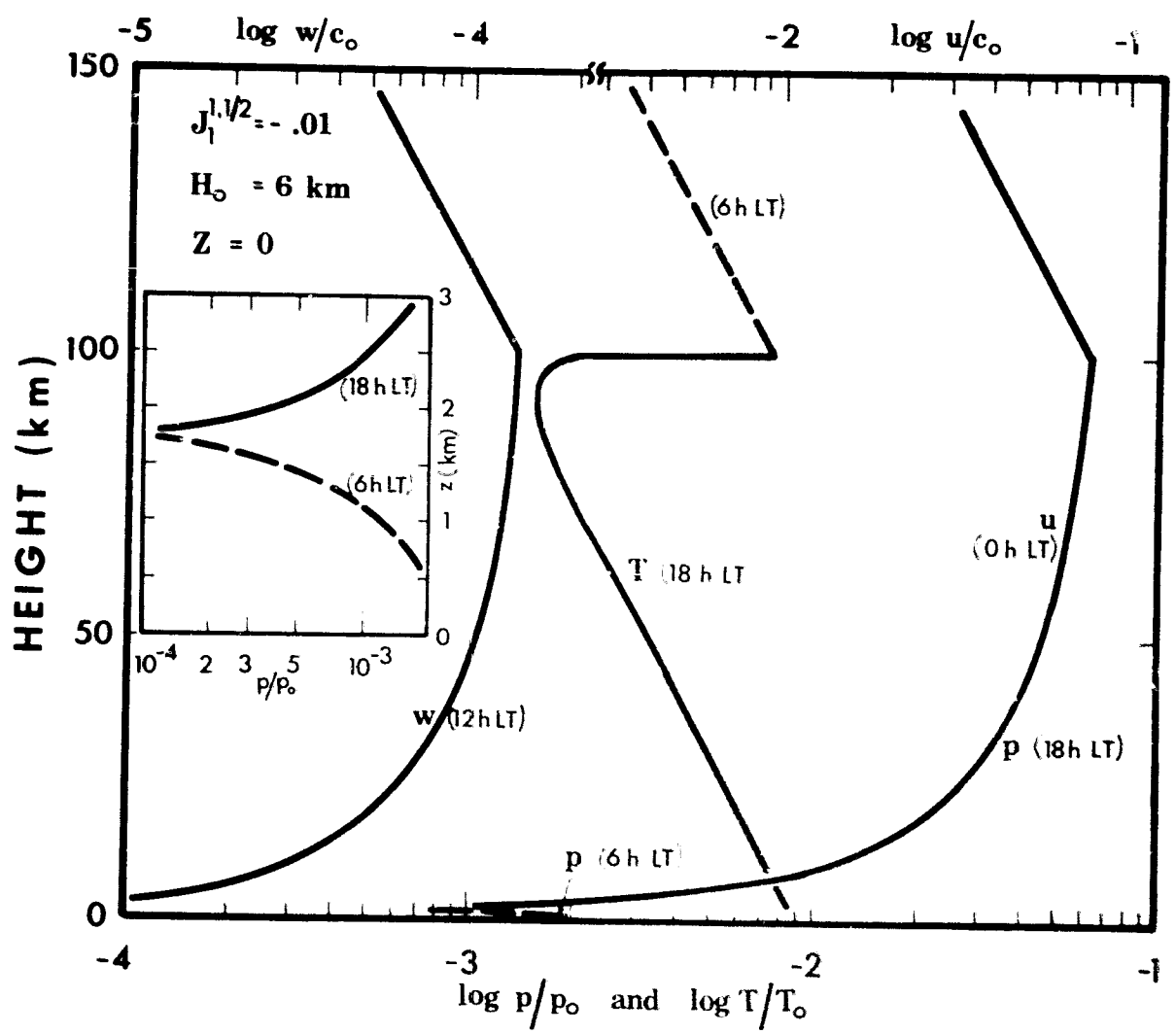

Figure 4. Relative wave amplitudes of pressure p, temperature T and vertical wind w versus altitude of the symmetric diurnal $\Theta_1^{1,1/2}$ -mode within the lower nondissipative atmosphere. The latitudinal velocity u is proportional to the pressure. Its pole values are given in the upper right scale. The time delay τ_o gives the time of maximum amplitude in local time. The heat peaks at local noon and is terminated at 100 km. Therefore above 100 km only upward propagating free internal wave exist. The pressure amplitude is zero at the height of the isobaric layer z_{isob} = 1.8 km and shifts in phase by 12 hours there (see the box on the l.h.s.)

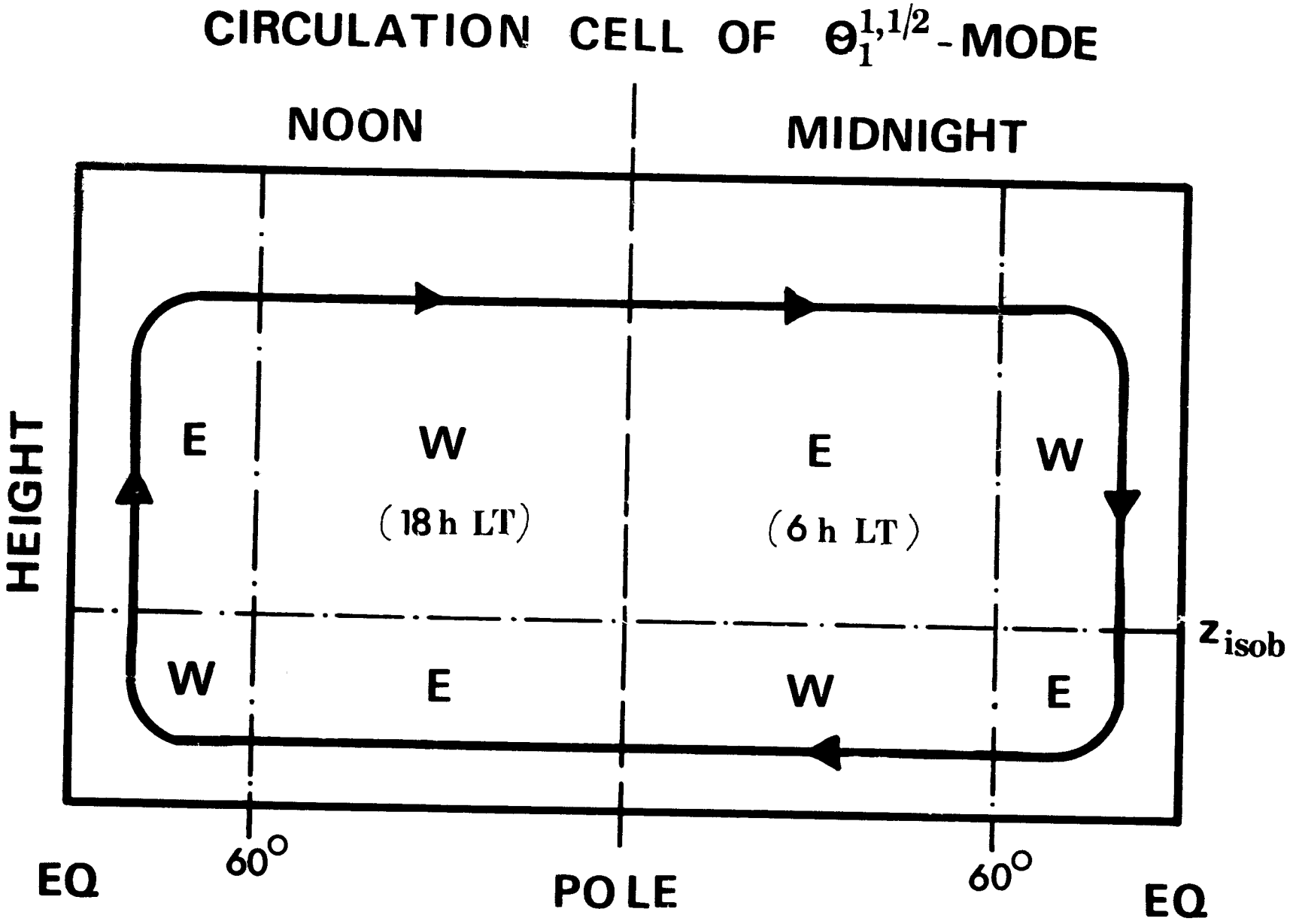

Figure 5. Non-midnight meridional cross-section of the wind system of the tidal $\Theta_1^{1,1/2}$ -mode within the lower atmosphere. The longitudinal winds are phase shifted by 6 hours with respect to the latitudinal winds. Maximum westerly winds (winds blowing from the west) are indicated by the sumbol "W", easterly winds (winds blowing from the east) are indicated by "E".

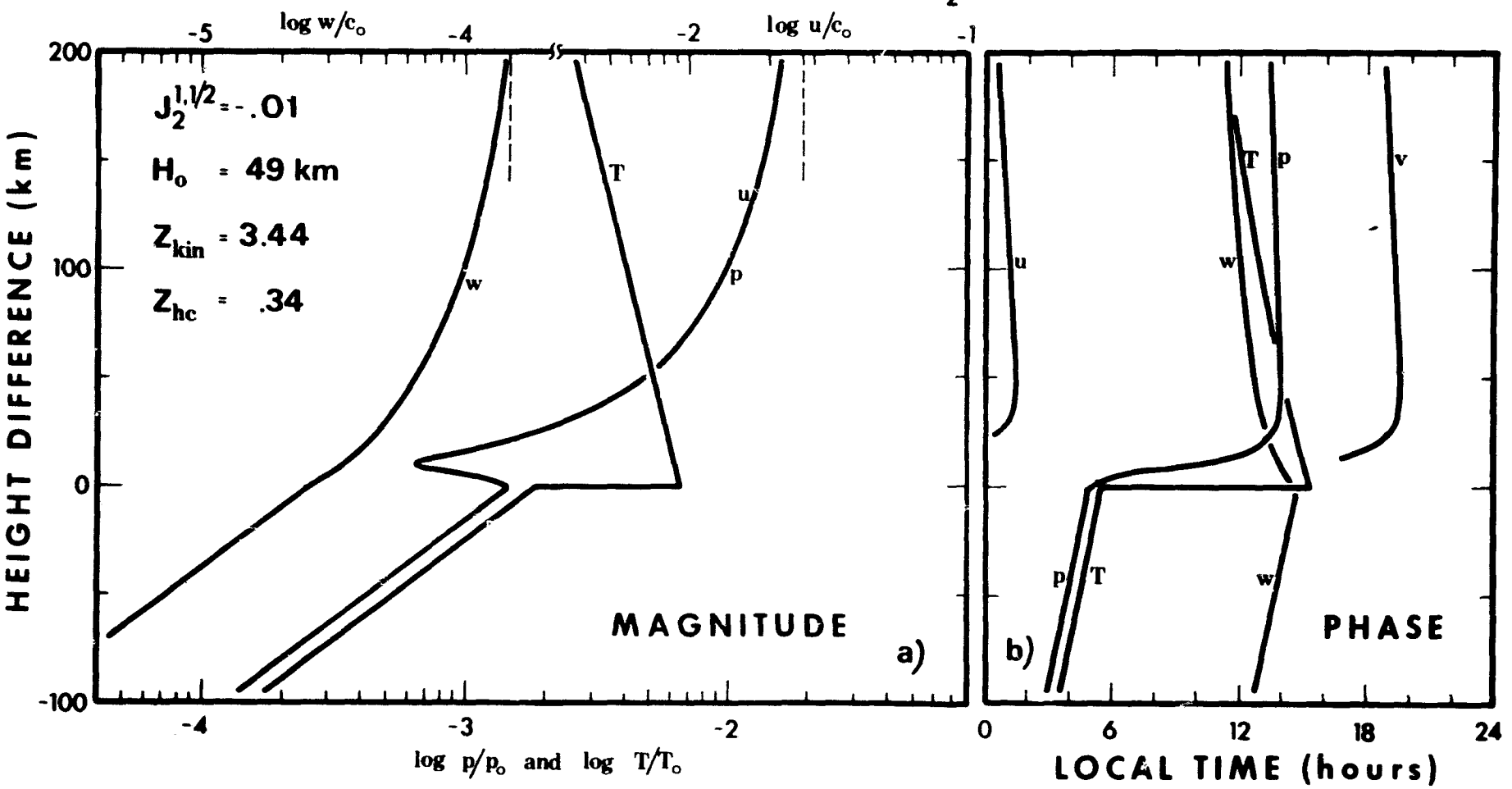

Figure 6. Relative wave amplitudes of pressure p, temperature T and vertical wind w versus altitude of the tidal $\Theta_1^{1,1/2}$ -mode within the dissipative thermosphere ($z_o \sim 200$ km). The generating heat input peaks at local noon and is terminated at the height z_o. Below that height only downgoing free internal waves exist.
Fig. 6a: magnitudes (the vertical dashed lines give the maximum asymptotic values of pressure and vertical wind).
Fig. 6b: times of maximum (in hours local time).

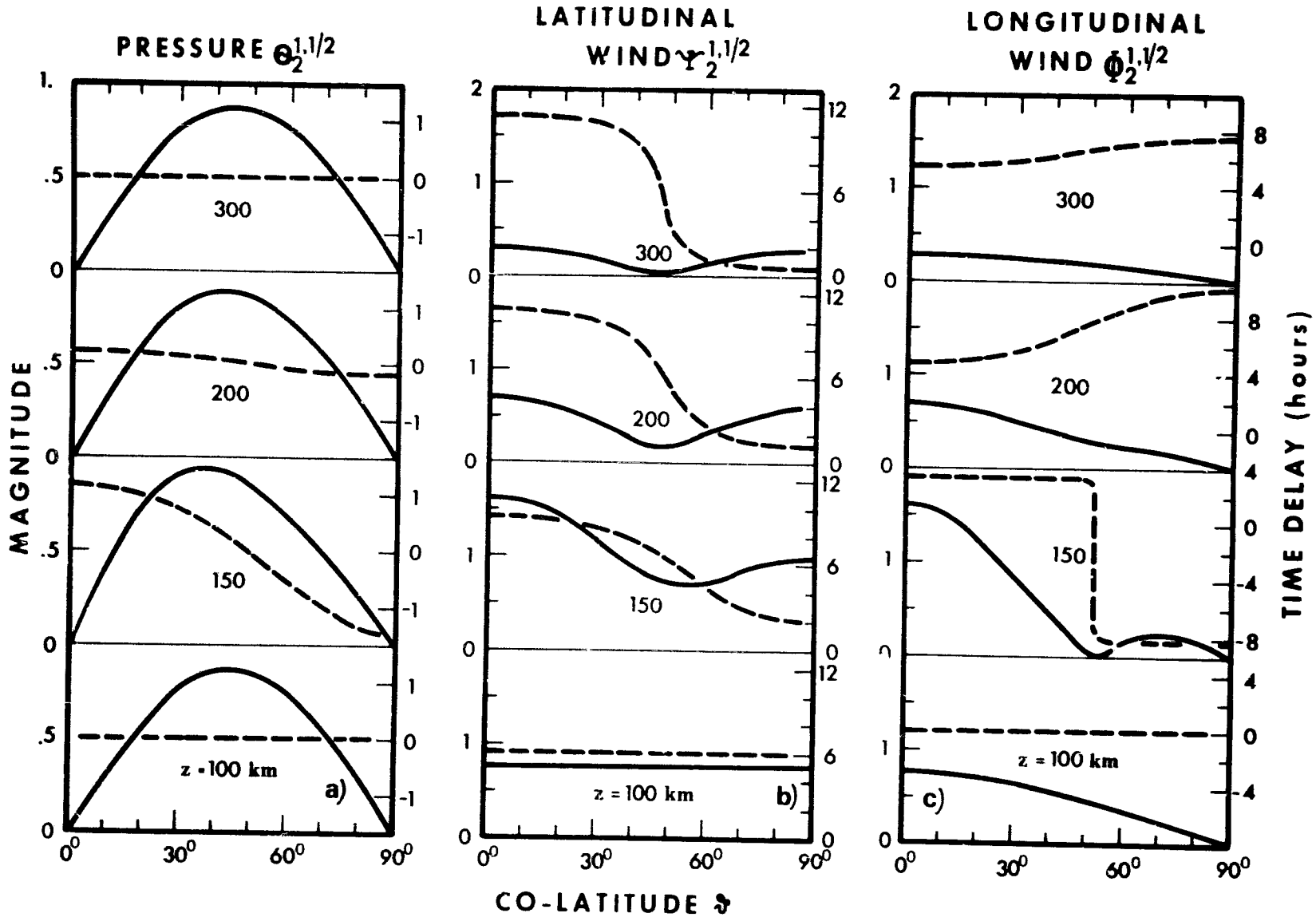

Figure 7. Dependence on co-latitude ϑ of the eigenfunction of the antisymmetric diurnal tidal $\Theta_2^{1,1/2}$ -mode for four different heights.
Fig. 7a: Pressure function $\Theta_2^{1,1/2}$ Fig. 7b: Latitudinal wind function $\Psi_2^{1,1/2}$ Fig. 7c: Longitudinal wind function $\Phi_2^{1,1/2}$

Solid lines: magnitude

Dashed lines: time delay (in hours)

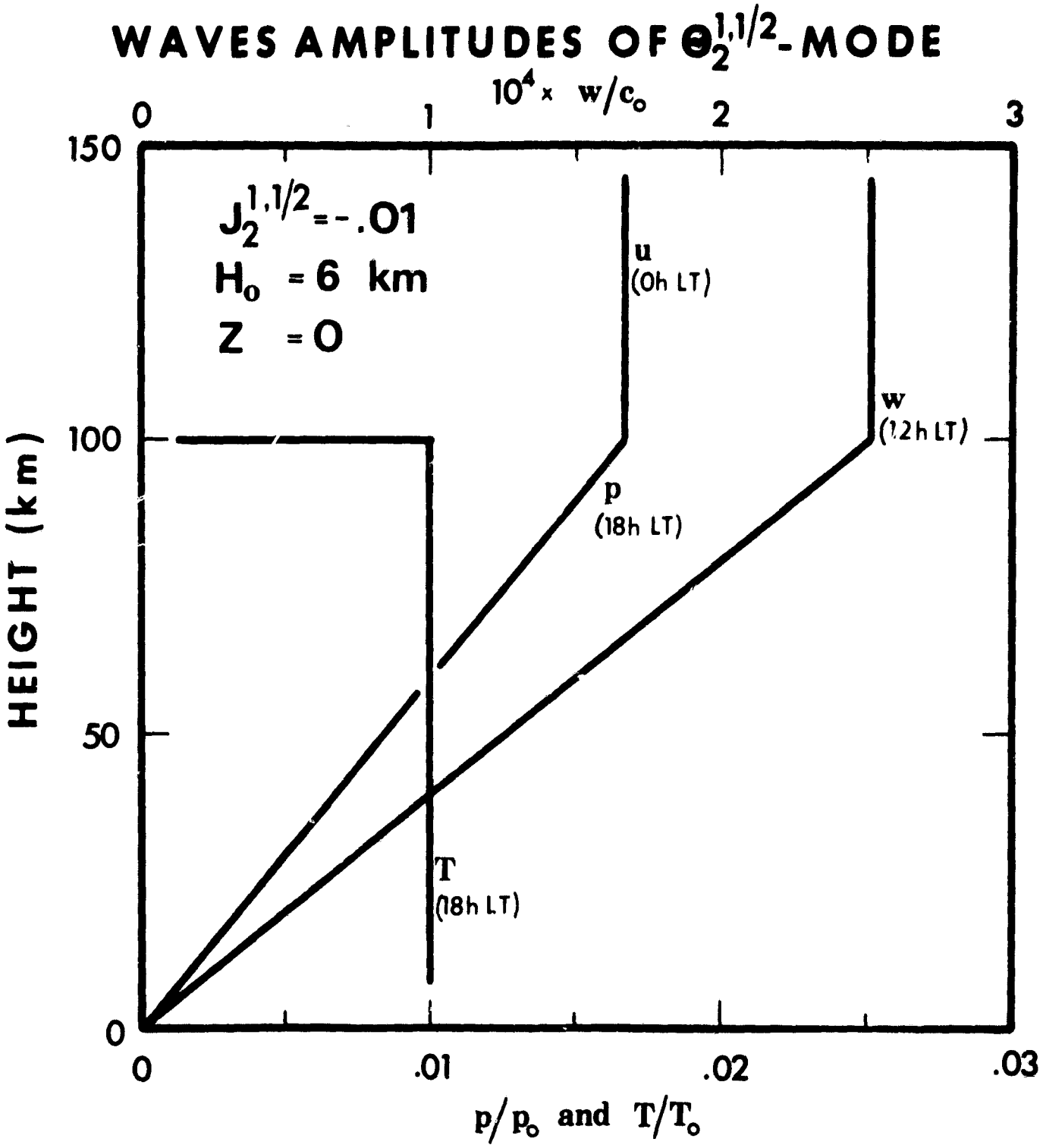

Figure 8. Relative wave amplitudes of pressure p, temperature T and vertical wind w versus altitude of the antisymmetric diurnal tidal $\Theta_2^{1,1/2}$ -mode within the lower nondissipative atmosphere and during June-solstice. The generating heat input peaks at local noon and is terminated at 100 km. The time delay τ_o gives the time of maximum amplitude in local time.

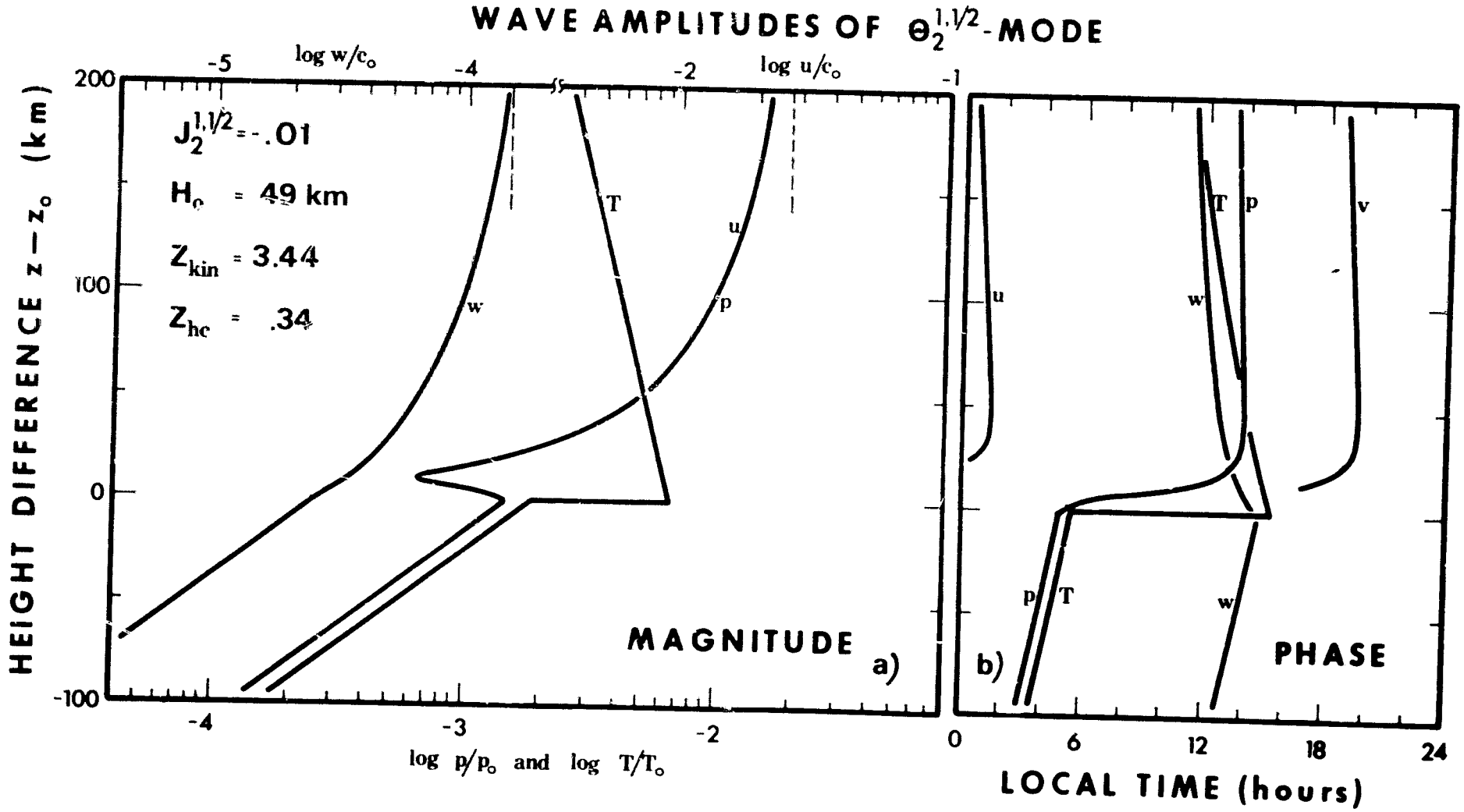

Figure 9. Relative wave amplitudes of pressure p, temperature T and vertical wind w versus altitude of the tidal $\Theta_2^{1,1/2}$ -mode within the dissipative thermosphere during June-solstice. The generating heat input peaks at local noon and is terminated at $z_o \sim 200$ km. Fig. 9a: magnitudes (the vertical dashed lines give the maximum assymptotic values of pressure and vertical wind). Fig. 9b: times of maximum (in hours local time).

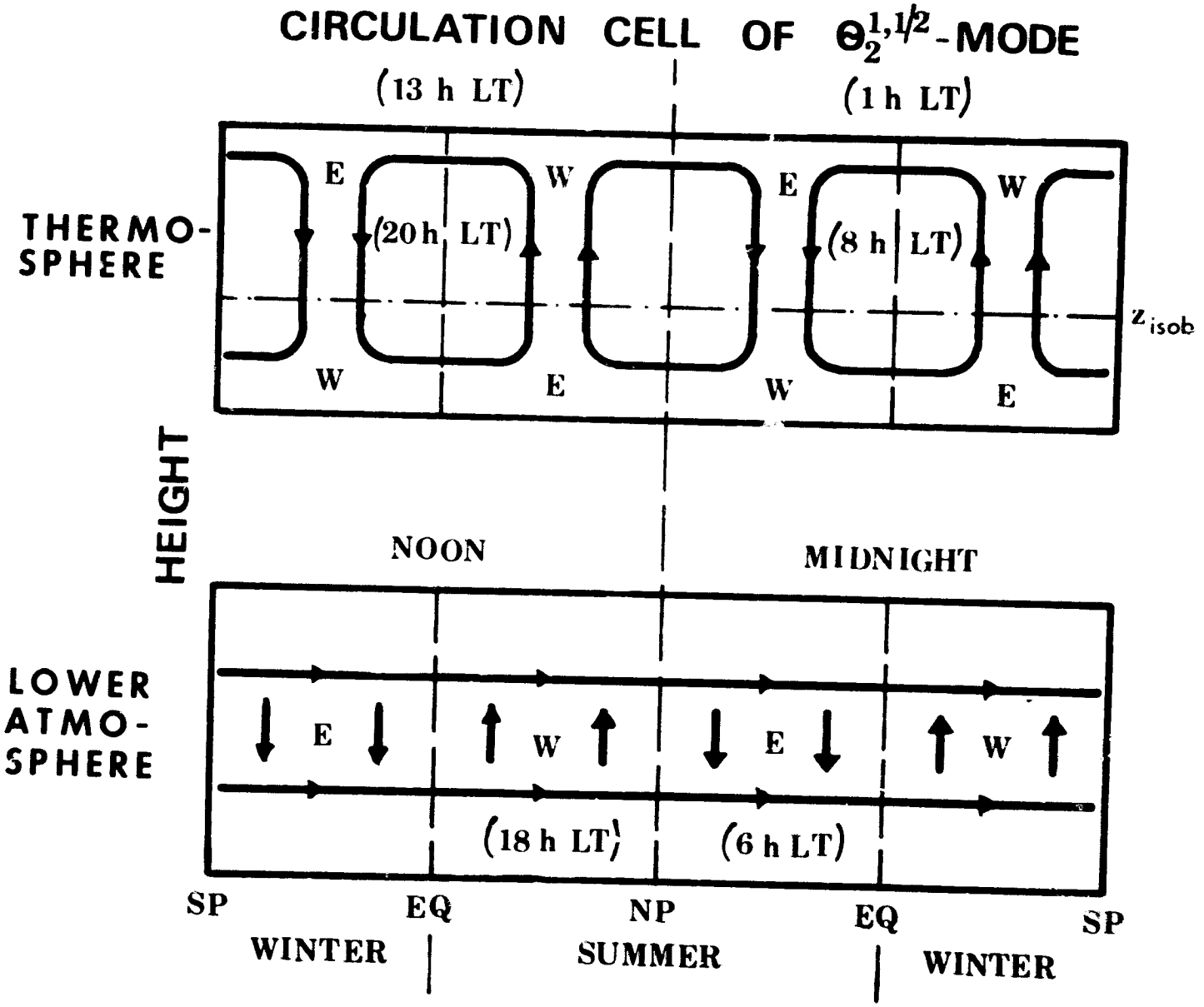

Figure 10. Meridional cross-section of the wind system of the tidal $\Theta_2^{1,1/2}$ -mode during June-solstice within the lower atmosphere and within the thermosphere. Maximum longitudinal winds phase shifted by about 6 h with respect to the meridional winds are indicated by "W" (westerly winds) and by "E" (easterly winds).

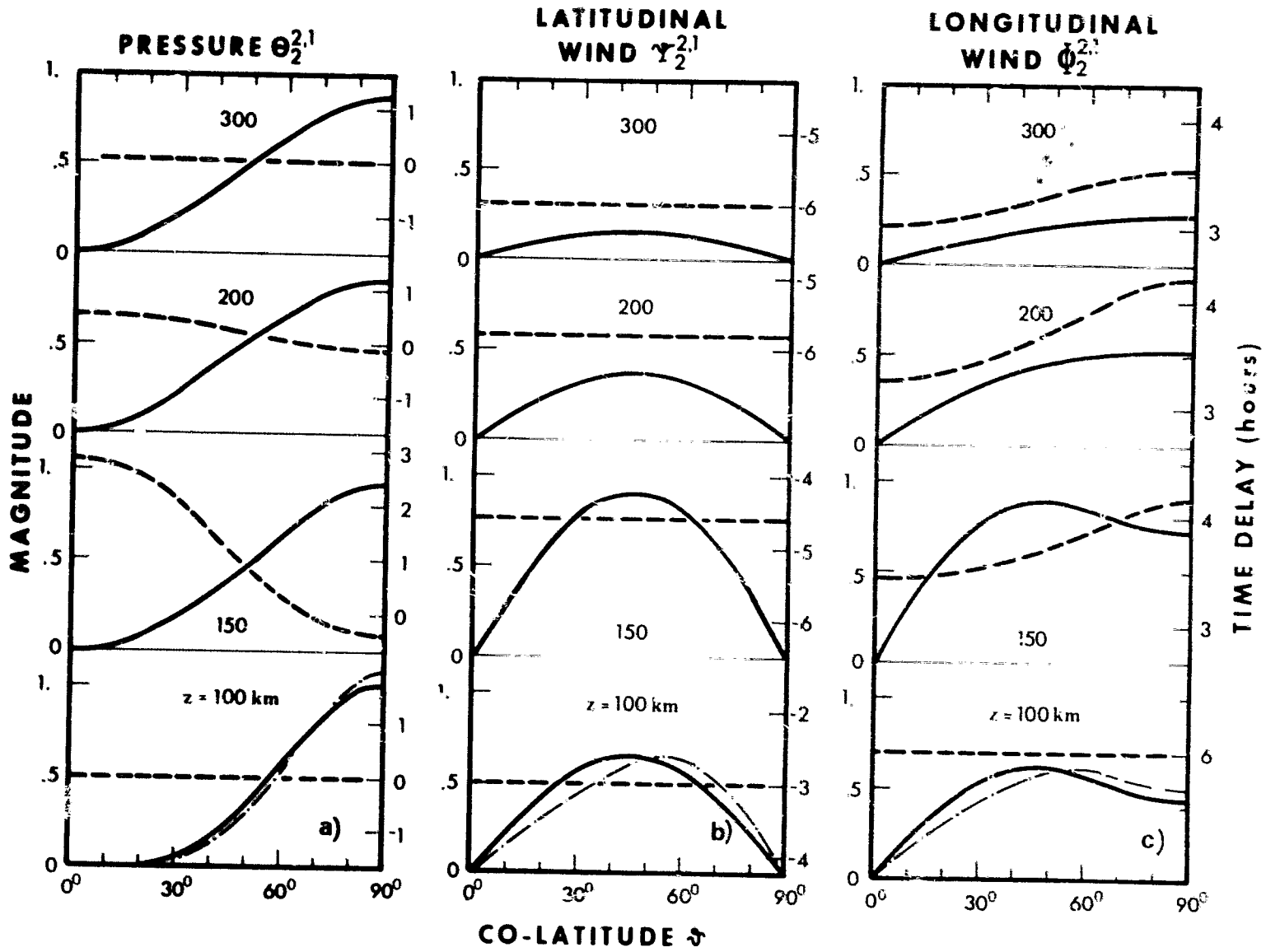

Figure 11. Dependence on co-latitude ϑ of the eigenfunction of the symmetric semidiurnal tidal $\Theta_2^{2,1}$ -mode for four different heights.
Fig. 11a: Pressure function $\Theta_2^{2,1}$ Fig. 11b: Latitudinal wind function $\Psi_2^{2,1}$ Fig. 11c: Longitudinal wind function $\Phi_2^{2,1}$

Solid line: magnitudes Dashed lines: time delay (in hours) Dash-dotted lines: exact values within the nondissipative lower atmosphere.

WAVE AMPLITUDES OF $\Theta_2^{2,1}$ - MODE

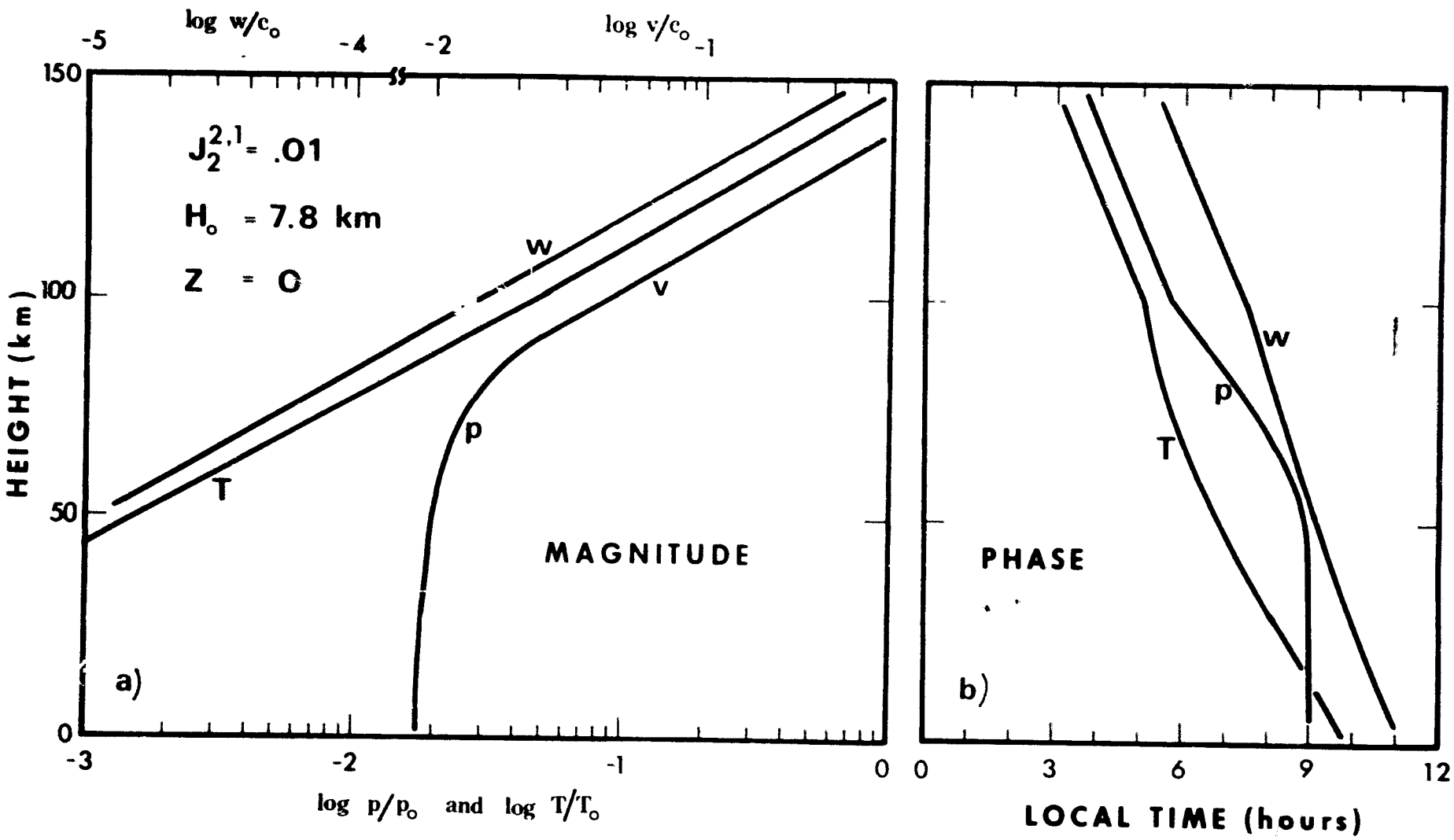

Figure 12. Relative wave amplitude in magnitude (Fig. 12a) and time of maximum in hours L. T (Fig. 12b) of pressure p, temperature T and vertical wind w versus altitude of the symmetric semidiurnal tidal $\Theta_2^{2,1}$ -mode w[illegible] the lower nondissipative atmosphere. The longitudinal wind v is proportional to the pressure. Its equator values are given in the upper right scale. The generating solar heat input peaks at local noon and midnight and is terminated at 100 km.

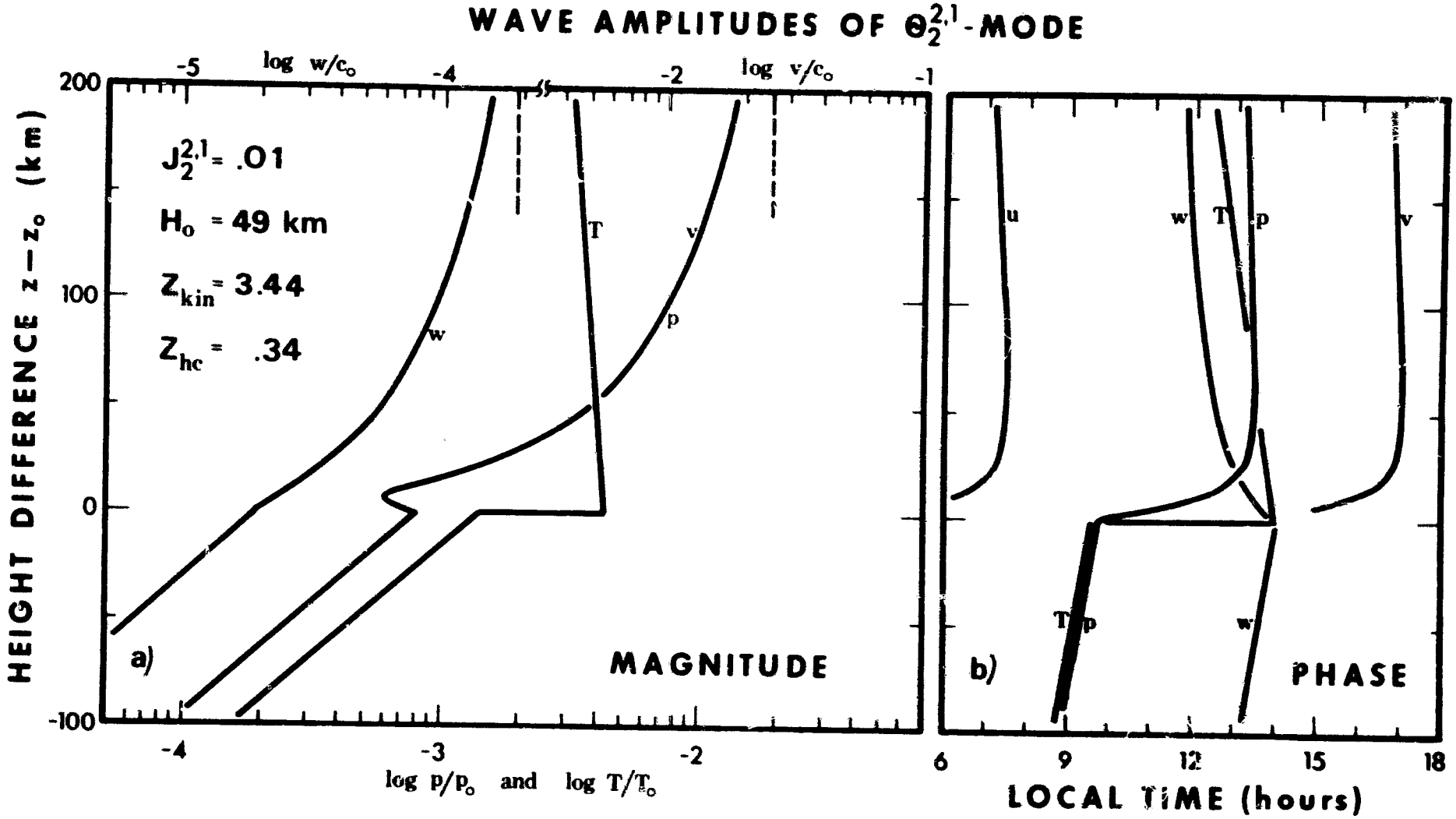

Figure 13. Relative wave amplitudes in magnitude (Fig. 13a) and time of maximum in hours local time (Fig. 13b) of pressure p, temperature T and vertical wind w versus altitude of the tidal $\Theta_2^{2,1}$-mode within the dissipative thermosphere. The generating solar heat input peaks at local noon and midnight and is terminated at $z_o \sim 200$ km.

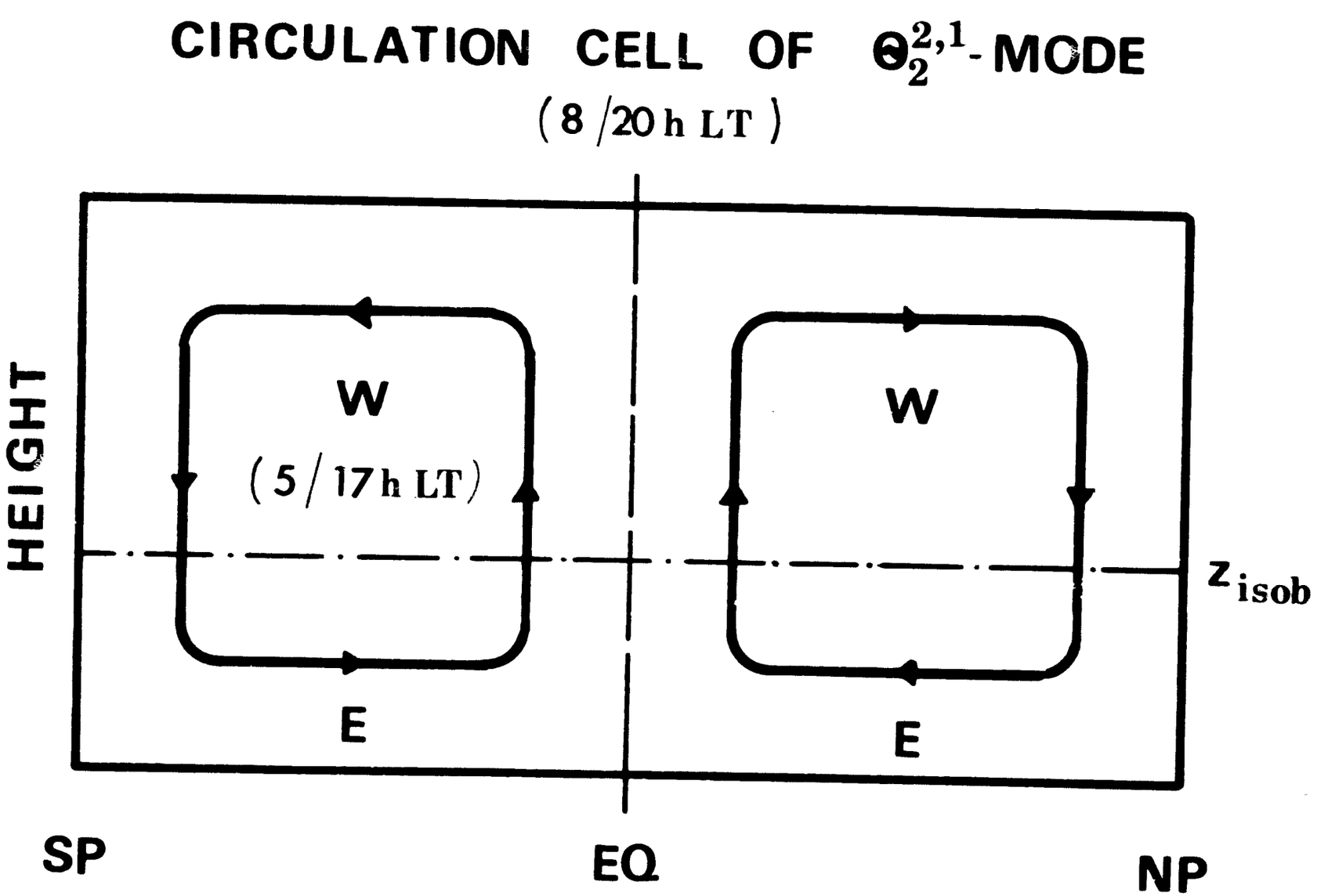

Figure 14. Meridional cross-section of the wind system of the tidal $\Theta_2^{2,1}$ -mode within the thermosphere. Maximum longitudinal winds phase shifted by about 3 hours with respect to the latitudinal winds are indicated by "W" (westerly winds) and by "E" (easterly winds).